Testing the state-dependent model of time perception against experimental evidence

Pirathitha Ravichandran-Schmidt [1,2,3,4,*], Joachim Hass [1,3,4,*]

1 Faculty of Applied Psychology, SRH University Heidelberg, Heidelberg, Germany
2 Faculty of Biosciences, University of Heidelberg, Heidelberg, Germany
3 Bernstein Center for Computational Neuroscience (BCCN) Heidelberg/Mannheim
4 Department of Theoretical Neuroscience, Central Institute of Mental Health, University of Heidelberg/Medical Faculty Mannheim, Mannheim, Germany

*pirathitha.ravichandran-schmidt.extern@srh.de (PR); joachim.hass@srh.de (JH)

Abstract

Coordinated movements, speech and other actions are impossible without precise timing. Computational models of interval timing are expected to provide key insights into the underlying mechanisms of timing, which are currently largely unknown. However, existing models have only been partially replicating key experimental observations, such as the linear increase of time, the dopaminergic modulation of this increase, and the scalar property, i.e., the linear increase of the standard deviation of temporal estimates. In this work, we incorporate the state-dependent model of time perception, which encodes time in the dynamic evolution of network states without the need for a specific network structure into a strongly data-driven prefrontal cortex (PFC). We show that this model variant, termed the state-dependent PFC model, successfully encodes time over several hundreds of milliseconds and reproduces all of the experimental results mentioned above. Furthermore, we propose a theory for the mechanism underlying time perception in this model, based on correlation and ablation studies as well as mathematical analyses. We show the representations of different intervals are based on the natural heterogeneity in the parameters of the network leading to stereotype responses of subsets of neurons to a stimulus at the end of each interval to be represented. The theory explains both the emergence of the scalar property of timing errors and of Vierordt's law, the fact that subjective duration is overestimated for short and underestimated for longer intervals. Overall, the state-dependent PFC model constitutes the first model of time perception in the range of hundreds of milliseconds that has been thoroughly tested against a variety of experimental data. As such, it provides an ideal starting point for further investigations of the mechanism of time perception.

Author summary

An accurate representation of time is crucial for a wide range of sensory, motor and cognitive tasks. Despite this importance, there is currently no commonly accepted theory for the mechanisms of time perception, although a wide range of modelling approaches exists. A possible reason for this discrepancy may be the fact that none of the existing models have been thoroughly tested against recurring experimental findings of time perception, such as the linear increase of subjective durations (psychophysical

law) and timing errors (Weber's law) with objective duration and the manipulation of subjective duration by dopamine. Here, we attempt to test one of the established models of time perception in this manner, namely the state-dependent model. We implement this model within a strongly data-driven network model of the prefrontal cortex and show that all the above-mentioned experimental findings are reproduced within a limited range of durations. We also offer a theoretical account for understanding the mechanisms underlying time perception in this model, with a focus on the emergence of Weber's law. Overall, the state-dependent PFC model represents the first model of time perception in the range of hundreds of milliseconds that reproduces the most prominent experimental findings of time perception.

Introduction

The ability to estimate the passage of time is of fundamental importance for perceptual and cognitive processes [95] such as speech, music, [11] and decision-making [9]. Impairments in time perception have been reported for various psychiatric disorders, such as schizophrenia, Parkinson's disease, Huntington's disease and major depression [10, 11, 51, 72, 82]. In mammalian neural circuits, time perception spans ten orders of magnitudes including millisecond timing, interval timing and circadian rhythms spanning an entire day [11, 73]. Among them, interval timing ranges from a few hundred milliseconds to several minutes and is involved in various processes as for instance foraging [49], decision-making [9], sequential motor performance [7] and associative conditioning [11, 29, 73].

Despite the importance of telling time, the exact neural mechanisms of time perception are not fully understood yet, in particular for interval timing. Proposing and testing biologically plausible computational models are a promising way to gain understanding of these mechanisms. A wide variety of models of time perception are currently discussed [41, 42], including the state-dependent network model [13], models of ramping activity [20] and synfire chains [44] as well as the striatal beat model [70, 74]. Despite this wealth of modelling approaches, none of them has currently been scrutinized in terms of their ability to reproduce key experimental findings of time perception. Furthermore, many of the existing models are strongly simplified, calling their biological relevance into question.

Here, we focus on the state-dependent network model [13], in which timing is not encoded by a dedicated tuning mechanism, but by the intrinsic neuronal and synaptic properties [52]. Specifically, the author claims that the representations of time up to 400 ms are generated by time-dependent mechanisms within the network, such as short-term plasticity and slow inhibitory postsynaptic potentials (IPSPs) caused by $GABA_B$ synapses [13]. More recent theoretical studies suggest that the hidden states of the network, induced by, e.g., short-term plasticity, allow to encode any stimulus together with its temporal context and time itself in the neuronal activity [14, 15, 52].

We aim to test whether this model may pose a plausible neural mechanism of time perception in the brain. To this end, we first implement the model into a strongly data-driven spiking network model of the prefrontal cortex [46] including substantial heterogeneities in the neuron and synapse parameters. Biological constraints, and heterogeneity in particular, has previously shown to pose a challenge to simple computational models, e.g., of working memory [48]. Second, we test whether the model can reproduce established experimental findings of time perception and can thus be validated by empirical data. This work is part of an ongoing research project that tests all of the above mentioned models in the same way as we test the state-dependent network model here. In the following, we introduce three important experimental findings of time perception the model will be tested against and explain why we chose

to use a model of the prefrontal cortex as a substrate of the timing model.

Timing is characterized by two fundamental properties, namely the linear psychophysical law for the average duration estimates [1, 5, 24], and the scalar property for timing errors, also referred to as Weber's law [11, 18, 31, 36, 67]. The linear psychophysical law states that real time is proportional to the averaged representation of time [24]. Although deviations from this linear relation have also been reported [25], calling for a power law generalization called Steven's law [25, 90], these deviations are small and the linear psychophysical law is still most widely accepted for time perception [1, 5]. However, the linear relation is not always a one-to-one relation. Already in the 19th century, Vierordt found that short intervals are overestimated, while longer intervals are underestimated [33, 96]. The indifference point varies depending on the intervals considered [64], e.g., employing intervals within the range of 200 - 1000 ms show the indifference point to be between 600 - 800 ms with the slope of timing of ~ 0.52 [56], whereas testing intervals within the range of 400 - 2000 ms, shifts the indifference point to higher values (~ 1400 ms) with a timing slope of ~ 0.86 [28]. Although some studies assume that the indifference point can be calculated by the arithmetic mean of the applied intervals [6, 28, 64], other studies do not support this hypothesis [64, 101, 103].

The scalar property refers to the observation that timing errors, or more specifically, the standard deviation of duration estimated between different trials, increases linearly with the duration of the interval to be timed. To quantify this relation, the Weber fraction can be used, dividing the standard deviation of the duration estimate by its mean. A constant Weber fraction over a range of durations is an indicator of Weber's law and has been observed in numerous studies. However, the scalar property is not universal, but seems to hold for intervals of around 200 ms [4, 27, 30, 35] up to 2000 ms [30, 100] in humans, with typical Weber fractions of around 0.05 - 0.13 [30, 37]. For shorter intervals, the Weber fraction increases, indicating a sublinear (e.g., square-root) scaling of timing errors, while for longer intervals, a superlinear increase of the timing errors and an increase of Weber fraction is reported (in humans, see [30, 100] and in animals [4, 16]). Using information-theoretical methods, Hass and Herrmann [43] suggested that these different scaling regimes of timing errors may indicate different mechanism underlying time perception. In particular, the scalar property is explained by so-called variance-based timing in this framework, i.e., using the temporal information contained in the timing errors itself, which increase over time and thus, can be used to decode time by means of a pure diffusion process.

While the linear psychophysical law and the scalar property constitute static properties of time perception, our sense of time is also highly variable in different situations and strongly depends on a number of factors, including emotions and mood [18], attention [80] and stimulus properties [22, 57, 98]. A prominent pharmacological modulator of time perception is dopamine [11, 83, 91]. Specifically, studies suggest that out of the two main types of dopamine receptors, D1 and D2, the latter one has a high potential to modify the subjective duration [71]. Numerous studies report that decreased dopaminergic activity, e.g., by dopaminergic antagonists, can slow down the internal clock leading to an underestimation of timing intervals, and increasing levels of dopamine, e.g., by dopaminergic agonists, speeds up the internal clock [11, 83, 91]. Furthermore, studies involving patients suffering from psychiatric disorders involving dopaminergic disbalance, such as schizophrenia [51, 72] and depression [10, 19], demonstrate altered performance in time discrimination tasks compared to healthy subjects [82]. A meta-analysis published by Thoenes and Oberfeld in 2015 shows a significantly reduced speed of the perceived flow of time in depressive subjects compared to non-depressive subjects [91]. Another study reveals that the positive symptoms of schizophrenia are related to an overestimation of timing intervals, leading to a speeding up of the internal clock [92].

A detailed biophysical model of the mechanisms of timing requires knowledge about the exact anatomical location of timing. While this location is still under debate [76, 99], fMRI studies suggest the involvement of prefrontal cortex, basal ganglia and striatum in timing processes ([66, 76, 99]). Various other studies are pointing towards the prefrontal cortex (PFC) especially in humans [53, 61] and also in animals [12, 60, 78, 102]. As the indications suggest an involvement of the PFC in timing, in this work, we implemented the state-dependent network model, proposed by Buonomano [13], within a strongly data-driven network model of the PFC [46] and tested whether this model can reproduce established experimental findings of timing, namely linear timing, scalar property and the dopaminergic modulation.

We found that the model successfully reproduces all three experimental findings outlined above within a limited range of interval durations. Thus, we further analyzed the underlying mechanisms based on the readout weights. We found that the network can be dissected into pools that represent a specific interval. In particular, neurons in each pool respond maximally to a second stimulus arriving after a given duration from the first stimulus has elapsed. This duration-specific response is mostly driven by their synaptic currents, e.g., short term plasticity and long-term $GABA_B$. Additional ablation studies confirm this hypothesis. Furthermore, limitations for longer interval durations and higher Poisson noise of up to a firing rate of 1000 Hz are examined to test the robustness of the model. Finally, we propose a theoretical account for the generation time perception following Weber's law within this model that also hints at possible generalizations beyond the particular model presented here and links violations of Weber's law with the occurance of Vierordt's law.

Results

Reproduction of experimental results

In order to test timing properties in a more realistic model, we incorporated the state-dependent model proposed by Buonomano [13] into the prefrontal cortex (PFC) [46] which was modified by including slow $GABA_B$ inhibitory currents [34]. All neurons of the state-dependent PFC network (Fig. 1) are stimulated in the beginning and in the end of an interval with a brief step current. The first stimulus was applied to the network at 1500 ms to guarantee that the network has reached a steady-state. After simulating the network, the number of spikes of each neuron within a time window, which is referred to as states, were extracted and the readout neurons were trained following the readout mechanisms of a liquid state machine [55, 68] (see Methods for details). We trained the weights of the readout units with various inter stimulus intervals (50 - 750 ms) in 50 ms steps and tested them with intervals (50 - 750 ms) in 25 ms steps. The normalized outputs of the trained readout units for different test intervals are shown in Fig. 2A. Each readout unit shows a tuning curve for its specifically trained intervals, allowing the model to generalize to intervals it has not seen during training. Testing an inter-stimulus interval in between two trained intervals, e.g. 125 ms, leads to a co-activation of the 100 ms and 150 ms readout unit. For test intervals longer than 300 ms, the tuning of the outputs becomes broader.

To test the linearity of the psychophysical law, we calculated the averaged subjective time by multiplying the output values of the readout units with their corresponding intervals and summing up over all readout units. As can be seen in Fig 2B, the estimated time is well described by a straight line (Fig 2B), as reported in experimental studies, with a fit error of $RMSE_t = 49.3 \pm 10.5$ ms. Furthermore, we observe an overestimation of shorter and an underestimation of longer interval (Fig. 2A), in agreement with Vierordt's law. Fitting the estimated time to a straight line

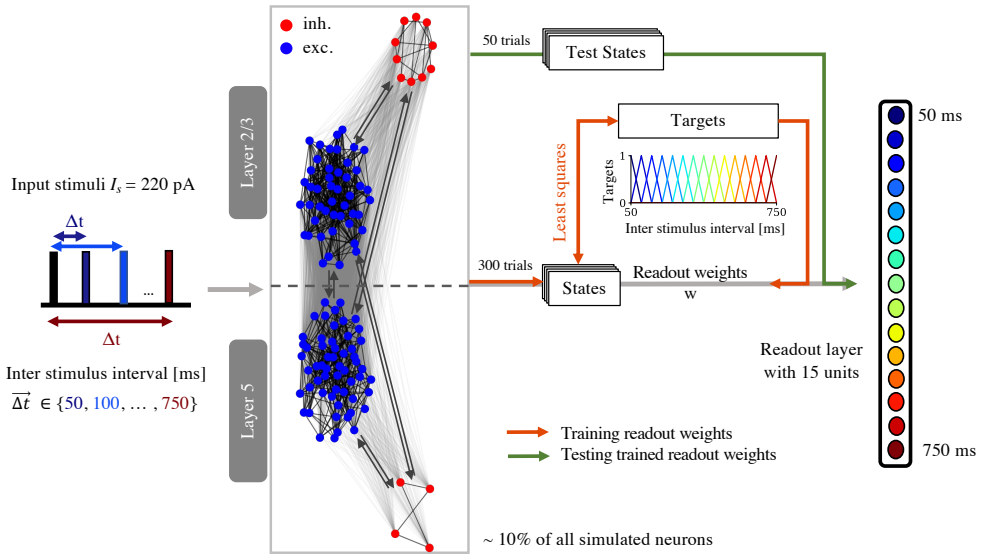

Fig 1. Illustration of the interval timing model. The PFC network (gray box in the middle) with layer 2/3 and layer 5 neurons (excitatory: blue, inhibitory: red, connectivities: gray arrows) is stimulated in the beginning and the end of several interstimulus intervals (color-coded from 50 ms to 750 ms). States (right to the network) are generated within a window from the spike trains, and the readout weights to the readout layer (same colors and number as inter-stimulus intervals) are trained via least-squares with the targets. Training is depicted with orange arrows and testing with green arrows.

($y = ax + b$), we get $a = 0.83 \pm 0.05$ and $b = 69.9 \pm 16.02$. The slope a is within the range of the experimental observations [28, 56] and significantly differs from 1.0, which corresponds to a one-to-one relation between subjective and objective time (one sample t-test: $t(49) = -24.06$, $p < 0.001$). The indifference point of the averaged estimated times can be found at IP = 530 ms, also in line with experimental studies [101].

To test the scalar property or Weber's law, we computed the evolution of the standard deviations of the estimated time over 50 trials, as shown in Fig. 2B and C. Fitting the data to a straight line as predicted by the scalar property, results in a root-mean squared error is $\mathrm{RMSE_l} = 3.5$ ms. We also computed the trial-averaged Weber fraction, restricted to the range of 400 - 750 ms (green line in Fig. 2D) to control for the fact that constant errors (the offset of the line) dominate at shorter intervals, causing the Weber fraction to decrease - a phenomenon that is well known under the term generalized Weber's law [4]. The Weber fraction of 0.059 matches experimental observations [30, 40]. To test if the data can be better fitted to the square-root function, this fit is additionally included (Fig. 2B in red), showing a slightly higher error of $\mathrm{RMSE_s} = 4.3$ ms.

Both properties, the linear psychophysical law and the scalar property, were further tested by using a number of sets of neuronal and synaptic parameters, each of which are randomly drawn from experimental validated distributions as in [46]. For ten parameter sets, the psychophysical law is well fitted by a linear function with an average fitting error of $\mathrm{RMSE_t} = 49.1 \pm 9.2$ ms, and a slope of 0.85 $\pm$0.05, which differs significantly from 1.0 (one sample t-test: $t(499) = -74.8$, $p < 0.001$). The indifference point of the averaged estimated time is 545.5 $\pm$ 23.3 ms.

Regarding the scalar property, Fig. 2C and the similar RMSE values for both types

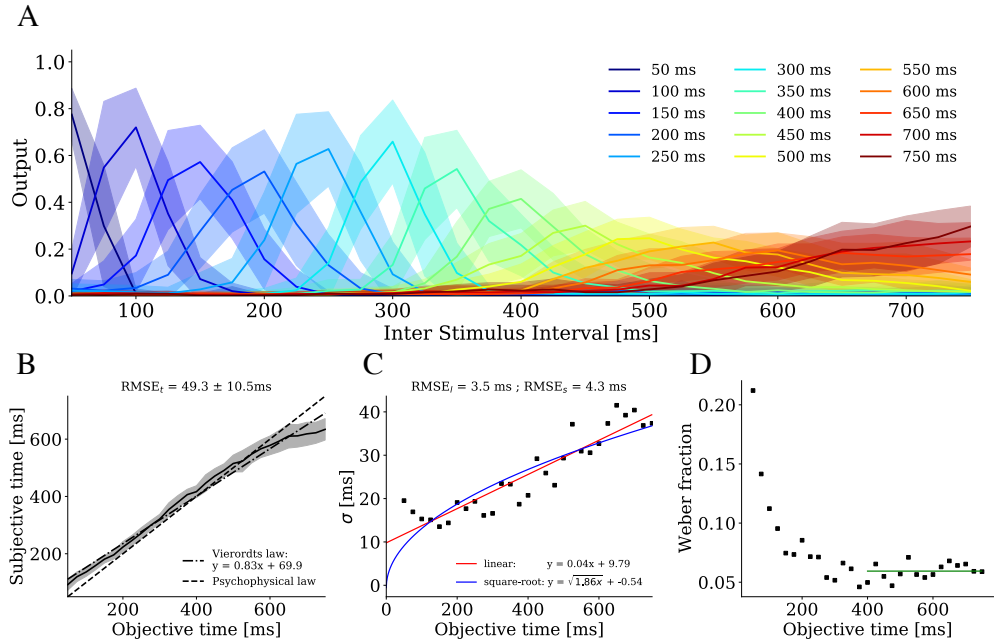

Fig 2. Psychophysical law and scalar property
A Illustration of the tuning curves of the readout units (color-coded) with standard deviation for different test intervals (x-axis). **B** Averaged subjective time (over 50 trials) as a function of test interval durations together with the standard deviations (shaded region), the linear fit (dashed-dotted-line) and the objective time (dashed black line). **C** Standard deviations of the estimated time as a function of test interval durations, fitted to a linear (red curve) and to a square-root function (blue curve). **D** The trial averaged Weber fraction as a function of test interval durations. The horizontal line depicts the average value between (400 - 750 ms).

of fit suggest that it is not trivial to determine whether the standard deviation follows a linear or a square-root function, i.e., whether the scalar property holds true. To clarify this issue, we repeated the simulations for the same ten parameter sets, but with a larger number of tested intervals (10 instead of 25 ms steps) and averaged the standard deviation across all parameter sets (Fig. 3). Up to interval durations up to 500 ms, the data is very well-fitted by a linear function. At longer intervals, however, the standard deviations saturate to a constant value. Overall, the data can be fitted by a piecewise linear function of the form

$$y = \begin{cases} a \cdot x + b & \text{for } x \leq c \\ a \cdot c + b & \text{otherwise} \end{cases} \tag{1}$$

with $a = 0.052 \pm 0.001$, $b = 10.6 \pm 0.4$ and $c = 530 \pm 8$. The fitting error RMSE_{pl} $= 1.22 \pm 0.04$ ms for this function is lower compared to both the linear ($y = ax + b$ with $a = 0.04 \pm 0.01$, $b = 13.88 \pm 1.55$, $\text{RMSE}_{\text{l}} = 2.47 \pm 0.14$ ms, paired t-test: $t(10) = -34.0$, $p < 0.001$) and square-root fits ($y = \sqrt{ax} + b$ with $a = 1.91 \pm 0.72$, $b = 2.56 \pm 2.93$, $\text{RMSE}_{\text{s}} = 2.14 \pm 0.11$ ms, paired t-test: $t(10) = -32.5$, $p < 0.001$). Fixing c at 500 ms yields only slightly different results, so the RMSE values can be compared despite the different numbers of parameters. Comparing Fig. 3 to Fig. 2B, one notices that the interval duration of 500 ms at which the standard deviation saturates coincides with the duration where the psychophysical law starts to deviate from a one-to-one relation with objective time. In a later section, we will see that these two deviations are

mechanistically linked.

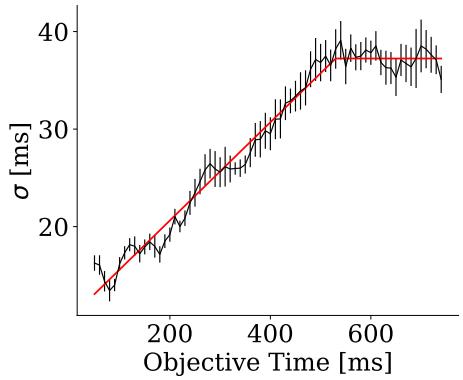

Fig 3. Assessing the scalar property
Standard deviations of the estimated time as a function of test interval durations, averaged across ten different parameter sets. The red line shows the best fit to a piecewise linear function, saturating for intervals above a threshold (see text for details).

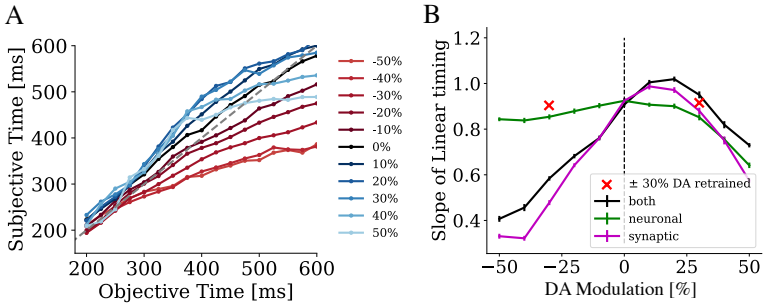

Fig 4. Effects of dopaminergic modulation
A Subjective duration as a function of test interval durations between 200 - 600 ms without modulation (black curve), for agonistic (blue curves) and antagonistic (red curves) D2 modulation. **B** The slope of the linear psychophysical law for each modulation for modulation of synaptic and neuronal parameters together (black curve), for synaptic modulation alone (magenta curve) and for neuronal modulation alone (green curve). The two red dots indicate slopes at -30% and +30% modulation after retraining of the readout weights. The vertical line indicates the point without modulation.

To examine the third experimental result, the modulation of subjective duration by the D2 dopamine receptor, we simulated a transient change of D2 receptor activation by changing the neuronal and synaptic parameters by the values summarized in Table 8, which reflect the experimentally observed effects of D2 *in vitro* (see Methods for details). These changes were only applied for the test phase, while for training, the same parameters were used as before. The changes in Table 8 were regarded as 100 % D2 activation (D2 agonist), while the original parameters reflected 0 % activation. Finally, inverting the sign of all the changes in Table 8 simulated −100 % D2 deactivation (D2 antagonist), so 0 % represented a baseline level of activation that can be increased or decreased. The full range of altered time estimates for DA modulation from 0 % to ±100 % for the test intervals of 50 - 750 ms are presented in Suppl. Fig. 1. As both agonistic and antagonistic modulation show boundary effects for DA modulations

$> \pm 50\,\%$ and for longer and shorter interval (Suppl. Fig. 1), we only considered intervals within a range of 200 ms - 600 ms and DA modulations up to $\pm 50\,\%$, see Fig 4A. The shift of the activation of the output neurons for increasing dopaminergic modulation is shown in the Suppl. Fig. 2 for the 400 ms encoding output neuron.

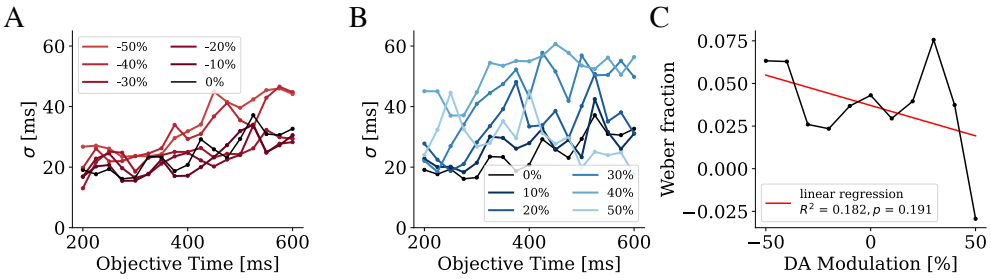

Fig 5. Scalar property after dopaminergic modulation
A Standard deviations of the estimated time as a function of test interval durations without modulation (black curve) and for antagonistic (red curve) D2 modulation. **B** Same as **A** without modulation (black curve) and for agonistic modulation (blue curves). **C** Weber fraction for each modulation together with a regression line (red line).

Within this limited range of durations and modulation levels, subjective time shortens for higher antagonistic modulations (Fig 4A, from darker to brighter red colors), and lengthens for agonistic modulation (Fig 4A, from darker to brighter blue colors), consistent with experimental results [11, 83, 91]. In Fig. 4B (black curve), we show the slope of a linear fit to the psychophysical law for each level of D2 modulation. The slopes reach a maximum around 20 % and drop again for higher values. The change in the slopes with the strength of dopaminergic modulation was statistically verified by an one-way ANOVA over 50 trials ($F(10, 539) = 299.3$, $p < 0.001$). To further assess the mechanism of D2 modulation of subjective time, we restricted the modulation to the synaptic (Fig. 4B, magenta curve) and the neuronal (Fig. 4B, green curve) parameters only. For the synaptic modulation, the slopes basically follow the same curve as with both modulations together, while the neuronal modulation alone only shows an effect at strong agonistic modulation, where it further decreases the slope.

Regarding the scalar property (Fig. 5), we also fitted a linear function to the data ($-50\,\%$ - $50\,\%$) for each modulation, but did not observe systematic changes in the slope (linear regression: slope = -0.0003, $p = 0.119$, $R^2 = 0.18$). The standard deviations and the slopes over the full range are shown in Suppl. Fig. 3.

If we retrain the readout weights under the influence of the D2 modulation, we can counteract the changing speed of the internal clock, as we tested on 30 % agonistic and antagonistic modulation. Fig.6 shows the psychophysical law and the Weber's law for agonistic dopaminergic modulation of 30 % (red, $\mathrm{RMSE_t} = 51.0 \pm 8.6$ ms with fitting parameters of $a = 0.82 \pm 0.04$ and $b = 71.92 \pm 14.27$ over the full range ($y = ax + b$) and with fit parameters of the piecewise linear fit: $a = 0.04$, $b = 11.5$ and $c = 650.0$), for the antagonistic dopaminergic modulation of $-30\,\%$ (blue, $\mathrm{RMSE_t} = 54.1 \pm 11.3$ ms with fitting parameters $a = 0.81 \pm 0.05$ and $b = 77.47 \pm 18.41$ over the full range ($y = ax + b$) and with fit parameters of the piecewise linear fit: $a = 0.04$, $b = 13.0$ and $c = 597.7$) and for the original case from Fig. 2B (black). Consistent with these results, a one-way ANOVA of the slopes of the psychophysical law did not show significant differences between the three cases ($F(2, 147) = 1.49$ and $p = 0.229$). The slopes for $\pm 30\,\%$ DA modulation after retraining the readout weights are shown in Fig. 4B as red dots.

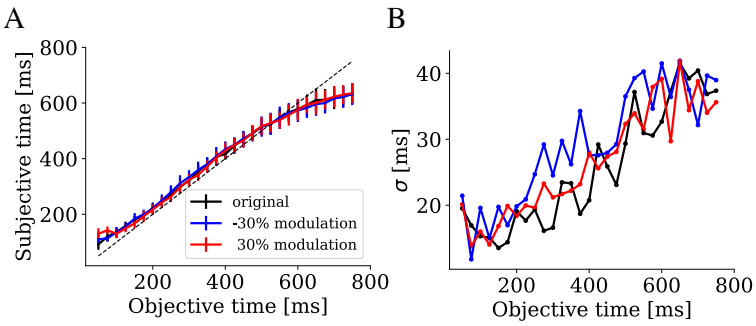

Fig 6. Retraining after mild dopaminergic modulation.
Estimated times (panel **A**) and the corresponding standard deviations (panel **B**) as a function of test interval durations for agonistic (30 %, red) and antagonistic modulation (−30 %, blue) after retraining. The estimated times and the standard deviations from Fig. 2 were re-plotted in black for comparison.

Limitations of the model

To examine potential limitations of the model, we considered longer intervals and higher noise levels. When we trained the readout network for longer interval durations up to 2000 ms and tested within the same range, we found that time perception was less accurate. In particular, the slope of the psychophysical law is much smaller compared to the original simulation, implying a more pronounced Vierordt's law (slope $= 0.66 \pm 0.07$, one sample t-test to compare to the identity ($t(49) =$ -35.57, $p < 0.001$), with the indifference point shifted towards longer intervals (IP = 852.9± 186.3 ms). Calculating the error with respect to the expected time yields $\mathrm{RMSE_t} = 264.0 \pm 43.4$ ms, cf. Fig. 7A. The fit error of the standard deviation to the piecewise linear fit is $\mathrm{RMSE_{pl}} =$ 28.7 ms with fitting parameters $a = 0.26$, $b = -3.9$ and $c = 615.0$, cf. Fig. 7B.

Table 1. Parameters for different noise levels with 1000 Hz Poisson neurons

		Psychophysical law			Scalar property		
$\mathrm{I_{back}}$ red.	weights	$\mathrm{RMSE_t}$	slopes	IP	piecewise linear fit		
[%]	[μV]	[ms]		[ms]	a	b	c
0 (1 Hz)	500	49.3 ± 10.5	0.83 ± 0.05	530.0	0.04	9.79	910.4
-7	3.0	69.3 ± 17.6	0.74 ± 0.08	472.0	0.05	14.2	625.0
-21	5.0	90.5 ± 23.4	0.67 ± 0.11	512.5	0.11	14.7	454.2
-36	7.0	107.9 ± 25.6	0.56 ± 0.12	477.7	0.12	13.5	452.5
-50	10.0	120.1 ± 30.2	0.52 ± 0.14	458.7	0.17	14.7	370.6

As a typical cortical neuron receives connections from approximately 1000-10 000 other neurons [8, 75], and we, so far, only tested with 10 Poisson neurons each with $f = 1$ Hz, we also examined whether time perception works at higher noise levels. To this end, we increased the firing rates of the 10 Poisson neurons to 1000 Hz and compared timing for different noise levels by increasing the weights of the Poisson neurons and simultaneously reducing the background current to avoid overexcitation and to keep the standard deviation of the sub threshold membrane potential constant, cf. Table 1 and Fig. 7C and D.

In these simulations, we find less accurate timing for increasing noise levels by increasing the synaptic weights from the 1000 Hz Poisson neurons onto the network. The linear timing error increases and Vierordts law becomes more pronounced, see Table 1. The piecewise linear function provides a good fit for the standard deviations

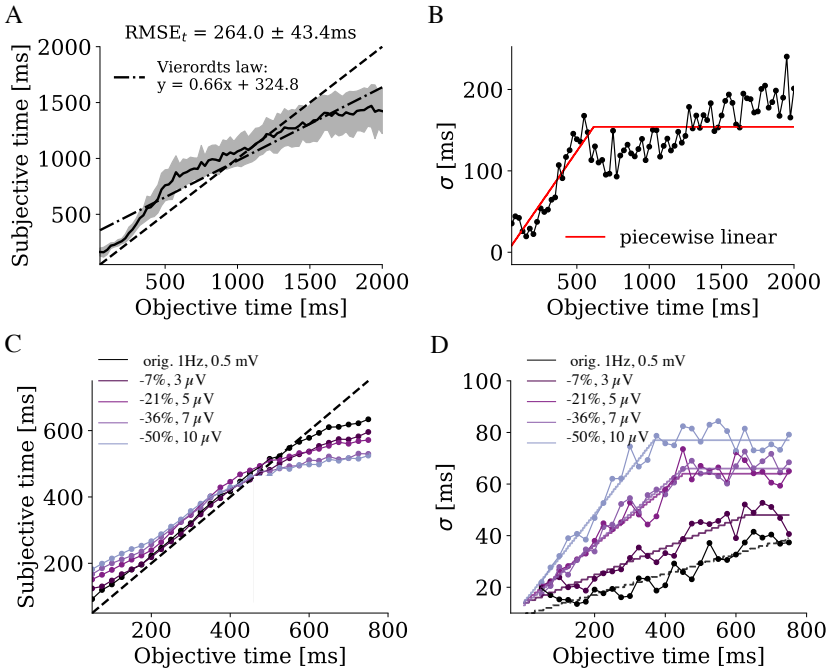

Fig 7. Testing for limitations of timing in the model.
Estimated time (panels **A, C**) and standard deviations (panels **B, D**) as a function of test interval durations for longer durations up to 2000 ms (panels **A, B**) and for higher noise levels (panels **C, D**). Lighter colors in panels **C** and **D** represent higher noise levels (see text and Table 1 for details).

with small fit errors $\mathrm{RMSE}_{\mathrm{pl}}$ (Table 1) as noise levels increase, but the cut-off value c is shifted towards shorter intervals for higher noise levels (see Fig. 7D).

Mechanisms of time perception

Given that time perception, especially Weber's law, works within the state-dependent PFC model at least for lower noise levels and intervals up to 750 ms, we next aimed for understanding the underlying mechanisms of timing within this model. In a first step, we performed correlation studies to determine whether there are pools of neurons that encode specific intervals and if yes, how they differ from non-predictive neurons and from neurons which are predictive for other intervals. As a next step, we performed ablation studies, i.e., systematically disabled specific components of the network to determine which of them are critical for which aspect of timing in our model. Furthermore, we studies a simplified model to explain the origin of the scalar property and Vierordt's law. In order to rule out other possible mechanisms, we additionally tested for the existence of sequential activation of groups, e.g., synfire chains, as well as ramping activity in the model.

Correlation studies

To identify potential interval-encoding pools, we assigned neurons to a single trained interval by finding the highest readout weight, as it was already done in [13] (see Methods for details). 242 neurons were not assigned to an interval-encoding pool (see Fig. 8A), as the readout weights of these neurons were 0 for all trained intervals. Since we wanted to understand the underlying mechanisms of these assigned neurons we only

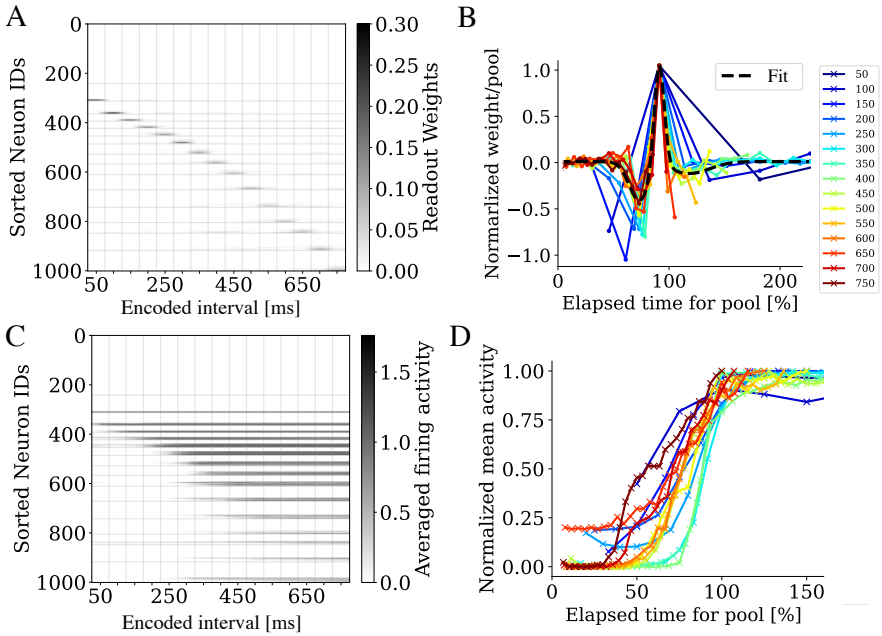

Fig 8. Readout weights and average firing rates within interval-encoding pools

A. Neuron IDs sorted by their strongest weights (coded by shades of grey) to a readout unit. **B** The normalized averaged readout weights of the neurons within a pool as a function of test interval durations, shown as a fraction of the encoded interval duration of each pool (color-coded by the readout intervals). The dashed line is the best fit of all curves. **C** The averaged states over 50 trials for the sorted neurons within a pool. **D** The normalized averaged activity within a pool for each test interval as a function of test interval durations, shown as a fraction of the encoded interval duration of each pool (color-coded as in **B**).

considered those neurons which had an high impact in the readout (weights above 0.01), and weights below 0.01 are set to zero for all following analyses.

After assigning the neurons to pools, the pools were sorted from shorter to longer intervals and within each interval-encoding pool, the neurons were additionally sorted from low to high weights, as shown in Fig. 8A. Calculating the normalized averaged weight distribution from the neurons in each pool to their respective readout neuron (before thresholding), we see stereotype weight profiles which we term *temporal receptive fields*: Weights peak shortly before the time that the respective pool represents and suppress contributions from both earlier and later pools in an asymmetric fashion (Fig. 8B). Furthermore, we compared the states of neurons in each poool in response to the second stimulus and also found a stereotype firing rate profile for most pools: the normalized firing rate increases until 100 % of the elapsed time for respective pool is reached and saturates for all longer intervals, see Fig. 8C and D. Taken together, these results indicate that each pool translates the time elapsed relative to the interval it represented into a similar firing-rate code and also transfers this code to its respective readout neuron using a stereotype weight profile.

Having thus confirmed the functional relevance of the interval-sensitive pools of neurons, the remainder of this section is concerned with the mechanism that underlie this sensitivity. To this end, we compared different parameters between the different pools. We call these analyses correlation studies in contrast to the experimental

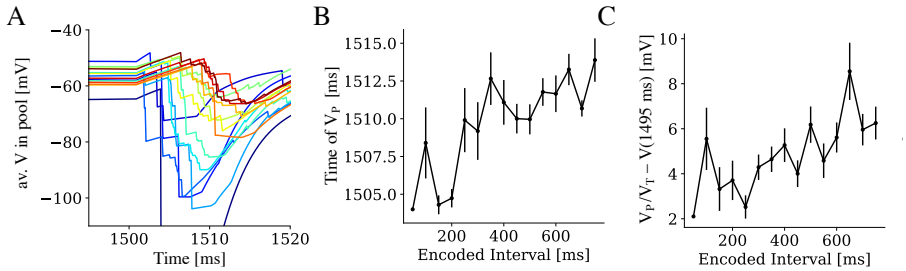

Fig 9. Pool averaged membrane potential of excitatory neurons.
A Averaged membrane potentials of excitatory neurons for each interval-encoding pool (color-coded as in Fig. 8B) as a function of simulation time. **B** Average time at which the peak potential V_P is reached for excitatory neurons in each pool as a function of the duration encoded in each pool during the first stimulation. **C** Difference of averaged membrane potential in excitatory neurons in each pool 5 ms before the first stimulation (i.e. $t = 1495$ ms) to firing threshold V_T (or peak potential V_P if the respective did not elicit any action potential) as a function of the duration encoded in each pool during the first stimulation.

manipulations performed in the following section. For comparison, we also analyse the same parameter for neurons with readout weights below the threshold of 0.01 (Suppl. Fig. 4). First, we compared the average membrane peak potential (V_p) of excitatory neurons within a pool during the first stimulation at $t = 1500$ ms, cf. Fig. 9A, finding a clear shift within the averaged time point at which the peak potential is reached towards later intervals (Fig. 9B, one-way ANOVA: $F(14, 168) = 2.43$ and $p < 0.01$, slope = 0.01). To determine whether the neurons encoding shorter intervals are selected by a smaller distance of the membrane potential to their firing threshold potential, we also calculated this distance 5 ms before the first stimulation $t = 1495$ ms. For the neurons which were already above threshold and for neurons which did not fire at all, we calculated the distance to the peak value within a range of 1500 - 1530 ms. Doing so, a linear trend with a slope of 0.005 for the excitatory neurons could be found (one-way ANOVA: $F(14, 168) = 3.04$, $p < 0.001$), see Fig. 9C. Hence, neurons representing shorter intervals are relatively closer to their respective thresholds in comparison to neurons representing longer intervals. This effect could not be seen within the excitatory neurons with readout weights below the threshold of 0.01 (one-way ANOVA: $F(14, 417) = 2.65$, $p = 0.001$ and slope = -0.002).

In a next step, we examined the sum of all synaptic currents affecting each pool, separated for excitatory and inhibitory currents, as shown in Fig. 10A and B. As expected, all synaptic currents peak during the first stimulus and again at the second stimulus. We compared the absolute amplitude of synaptic currents before the first stimulus (Fig. 10C, averaged over the time between 1000 to 1500 ms), in response to the first stimulus (Fig. 10D) and the second stimulus (Fig. 10E) and found an increase in both excitatory and inhibitory currents for pools encoding longer intervals in all three cases (Fig. 10C, D and E). This linear effect is most pronounced for intervals up to 400 ms, but still was statistically verified for the whole range of intervals, see Table 2. In contrast, the total current (the sum of excitatory and inhibitory currents) did not change systematically across pools encoding different intervals (see Table 2, except for the total current before stimulation).

In order to determine whether the excitability of the neurons varies between different pools, we calculated the averaged rheobase for each pool (Fig. 11A) and subtracted this value from the averaged total synaptic current within the range 1000 ms - 1495 ms, cf. black line in Fig. 10C. Although neither the rheobase (one-way ANOVA:

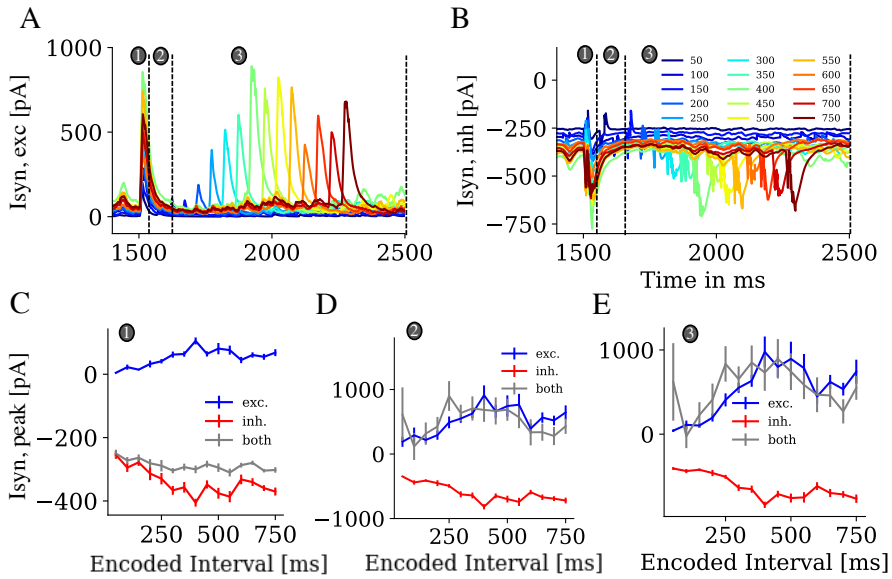

Fig 10. Synaptic currents within the pools.
The averaged excitatory (panel **A**) and inhibitory (panel **B**) synaptic currents of the neurons within each pool as a function of simulated time. The three circles and the dashed lines mark the three time points at which the synaptic currents are compared, namely before stimulation (1, panel **C**), during first stimulation (2, panel **D**) and during the second stimulation (3, panel **E**). For each case, average excitatory (blue curves), inhibitory (red curves) and the overall currents (grey curves) are shown for each pool as a function of the duration encoded in each pool.

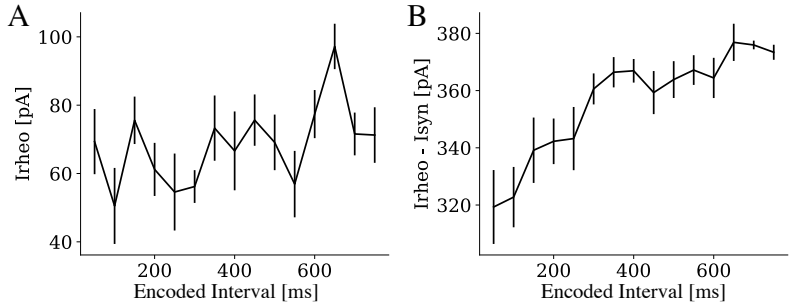

Fig 11. Excitability of interval-encoding pools
A Averaged rheobase (see Methods for details) and **B** the difference of the rheobase to the total synaptic current within each pools before stimulation as a function of the duration encoded in each pool, cf. black line in Fig. 10C.

$F(14, 200) = 1.63$, $p = 0.07$, slope $= 0.024$, $R^2 = 0.23$, $p = 0.073$) nor the total synaptic current (Table 2 - before stimulation, both) differs between pools, the difference of the two does increase over the whole interval range between 50 and 750 ms (linear regression: slope $= 0.075$ and $R^2 = 0.82$, $p < 0.001$ and one-way ANOVA: $F(14, 200) = 5.10$, $p < 0.001$), see Fig. 11B, implying that a higher overall current is needed to make the neurons in pools encoding longer intervals fire. In contrast, if we consider only those neurons within the pools below the weight threshold of 0.01, the difference of the rheobase to the synaptic current does not depend on the preferred

interval duration (slope = 0.065 and $R^2 = 0.20$, $p = 0.098$ and one-way ANOVA: $F(14, 530) = 2.1$, $p = 0.01$).

Table 2. Synaptic currents onto interval-encoding pools

Stimulation	one-way ANOVA 50 - 750 ms	linear regression 50 - 400 ms
before		
Exc. currents	$F(14, 200) = 3.89, p < 0.001$	slope = 0.25, $R^2 = 0.90$, $p < 0.001$
Inh. currents	$F(14, 200) = 4.50, p < 0.001$	slope = -0.39, $R^2 = 0.93$, $p < 0.001$
Both	$F(14, 200) = 1.34, p = 0.19$	slope = -0.14, $R^2 = 0.83$, $p < 0.01$
first		
Exc. currents	$F(14, 200) = 2.43, p < 0.01$	slope = 1.89, $R^2 = 0.87$, $p < 0.001$
Inh. currents	$F(14, 200) = 6.09, p < 0.001$	slope = -1.19, $R^2 = 0.88$, $p < 0.001$
Both	$F(14, 200) = 1.22, p = 0.26$	slope = 1.16, $R^2 = 0.33$, $p = 0.14$
second		
Exc. currents	$F(14, 200) = 3.92, p < 0.001$	slope = 2.55, $R^2 = 0.91$, $p < 0.001$
Inh. currents	$F(14, 200) = 6.84, p < 0.001$	slope = -1.14, $R^2 = 0.85$, $p < 0.001$
Both	$F(14, 200) = 1.51, p = 0.11$	slope = 1.63, $R^2 = 0.42$, $p = 0.08$

So far, we analyzed the dynamic membrane potentials and the synaptic currents to understand the mechanisms of time perception. Next, we examined whether the assignment of a neuron to one of the interval-encoding pools can also be predicted based on the static neuronal and synaptic parameters alone. To this end, we conducted a linear discriminant analysis to assess a) which variables are most important to separate the pools encoding different intervals and b) which variables differentiate between those neurons that are predictive for any interval and those that are not. Regarding neuron parameters, we concentrated on the rheobase, the membrane time constant (computed as $\tau_m = C_L/g_L$) and the time constant of the adaptation current t_w (see Methods for details). For the synaptic parameters, we consider all synapses that project onto a given neuron and differentiate between excitatory and inhibitory synapses. For each synapse type, the averaged synaptic weight and delay as well as the three parameters of short-term synaptic plasticity (U, t_{rec} and t_{fac}) are considered, together with the number of excitatory and inhibitory synapses that are projecting onto the cell.

In the first discriminant analyses, we used the above-mentioned variables to predict which interval within the range between 50 and 500 ms each given neuron encodes. The analysis (using z-scores of all 15 independent variables) yields three discriminant functions that separate between the intervals significantly. However, we concentrate on the first function only as it contains 76% of the discrimination potential, while the other two only add 10% and 7%, respectively. The first function takes significantly larger values for neurons that represent longer intervals (Wilk's lambda: 0.55, $\chi^2(135) = 841.1, p < 0.01$). The structure matrix (Table 3) reveals that, among the synaptic parameters, both the inhibitory and excitatory weights, the number of inhibitory synapses projecting onto the neuron, the synaptic delay of the excitatory and the STP time constants of the inhibitory synapses are most important for differentiating between the different intervals. Among the neuronal parameters, the membrane time constant and the rheobase are most important for the differentiation.

In the second analysis, we used the same independent variables to predict whether a given neuron encodes any specific interval or not. The analysis yields a single discrimination function with significantly higher values for interval-encoding neurons compared to neurons that do not encode any interval (Wilk's lambda: 0.958, $\chi^2(15) = 473.2, p < 0.01$). The structure matrix (Table 4) identifies the rheobase, the number of excitatory and inhibitory neurons as well as the synaptic delays for both

types of synapses as the most important discriminating variables in this case.

Table 3. Discriminant function analysis between interval selective pools

Type	Z-score	linear regression		
		slope	R^2	p
weights inh. synapses	.849	-0.46	0.96	< 0.001
weights exc. synapses	.686	2.28	0.90	< 0.001
connectivity inh. synapses	.611	0.06	0.88	< 0.001
synaptic exc. delays	.561	0.001	0.83	0.002
$\tau_{\mathrm{rec,Inh}}$	.560	-0.97	0.51	0.045
$\tau_{\mathrm{fac,Inh}}$	-.559	0.98	0.52	0.045
$\mathrm{I_{rheo}}$	.463	0.007	0.009	0.82
$\tau_{\mathrm{mem}} = \mathrm{C_m/g_L}$	.429	0.03	0.72	0.008
$\mathrm{U_E}$	.295	0.00005	0.93	< 0.001
$\tau_{\mathrm{rec,Exc}}$	-.201	-0.35	0.83	0.002
$\mathrm{U_I}$	.190	0.00006	0.58	0.03
$\tau_{\mathrm{fac,\ Exc}}$	.187	0.3	0.85	< 0.001
connectivity exc. synapses	-.181	0.78	0.66	0.014
τ_{w}	.143	0.04	0.20	0.27
synaptic inh. delays	-.039	0.00	0.03	0.66

Table 4. Discriminant function analysis between selective and non-selective neurons

Type	Z-score
$\mathrm{I_{rheo}}$	-.580
connectivity exc. synapses	.545
connectivity inh. synapses	-.498
synaptic exc. delays	-.441
synaptic inh. delays	-.397
$\tau_{\mathrm{fac,Inh}}$	.284
weights exc. synapses	.264
$\tau_{\mathrm{rec,Inh}}$	-.177
τ_{w}	-.156
$\mathrm{U_I}$	-.107
$\mathrm{U_E}$	-.091
$\tau_{\mathrm{mem}} = \mathrm{C_m/g_L}$	.068
weights inh. synapses	-.062
$\tau_{\mathrm{rec,Exc}}$	.051
$\tau_{\mathrm{fac,Exc.}}$	-.040

We further explored the role of the above-mentioned variables for discriminating between interval durations (up to 400 ms) by plotting their mean values for each pool against the interval duration that is represented by that pool and test whether a linear regression with the durations yields a slope that is significantly different from zero, see Table 3. Indeed, the membrane time constant for both neuron types cf. Fig. 12A, as well as the facilitating time constants within the excitatory, Fig. 12B, and inhibitory neurons, Fig. 12C all show an absolute increase with duration of the encoded intervals in the respective pools, up to $\sim$ 400 ms. Simultaneously, the fraction of the depressing time constants are decreased up to $\sim$ 400 ms, cf. Fig. 12B for excitatory neurons and C for inhibitory neurons. Similarly, linear regressions were calculated for the summed

synaptic weights onto the neurons within each pool (black: slope = 1.82, R^2 =0.85, $p = 0.001$), positive (blue) and negative (red) weights, cf. Fig. 12D, for the number of inputs to each neuron (e.g. connectivity) (black: slope = 0.84, $R^2 = 0.70$, $p = 0.009$), positive (blue) and negative (red) cf. Fig. 12E and for the averaged synaptic delays onto the neurons within each pool (black: slope = 0.001 , $R^2 = 0.88$, $p < 0.001$), positive (blue) and negative (red) cf. Fig. 12F, of which the synaptic delays of the negative weights are not significant, which is consistent with Table 3. In contrast to the discriminant analysis, we find a non-significant increase in the rheobase within the subrange, although the structure matrix of the first reveals a strong score, showing that both analysis to not necessarily need to yield identical results for each parameter.

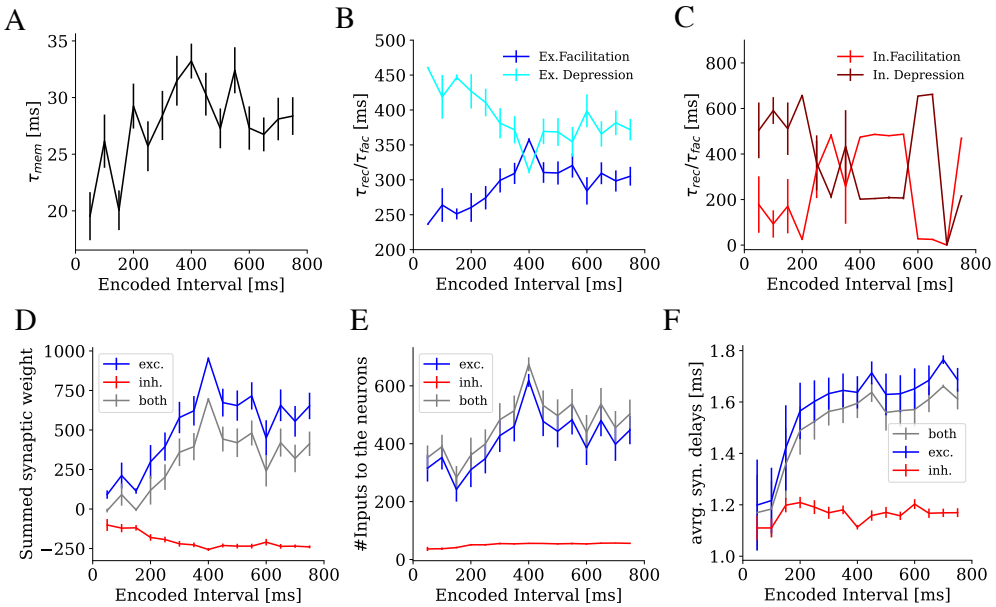

Fig 12. Neuronal and synaptic properties within interval-encoding pools
A Averaged membrane time constants τ_{mem} for both neuron types within each pool as a function of the duration encoded in each pool. **B** Averaged time constants of short term facilitation (τ_{fac}) and depression (τ_{rec}) for excitatory neurons within each pool as a function of the duration encoded in each pool. **C** Same as **B** for inhibitory neurons. **D** Averaged synaptic weights onto all neurons within each interval-encoding pool as as function of the duration encoded in each pool for positive weights only (blue curves), negative weights only (red curves) and all weights (grey curves). **E** Same as in **D** for the number of inputs. **F** Same as in **D** for the average synaptic delays.

As the same linear trends are not pronounced for neurons within the pool below the threshold, see Suppl. Fig. 4, these properties might be important factors for encoding time in our model. When linear regressions were calculated for the neurons below the threshold within the range of 50 - 400 ms, only the averaged synaptic delays of inhibitory neurons become significant (red: slope = -0.0002, $R^2 = 0.62$, $p = 0.02$), the remaining parameters are not significant.

Ablation experiments

In this section, we analyze which of the components of the model are critical for our results by systematically removing them. We focus on three main ingredients, namely synaptic processes with long time constants, heterogeneity of neuronal and synaptic

parameters and irregular background activity (induced by constant background currents).

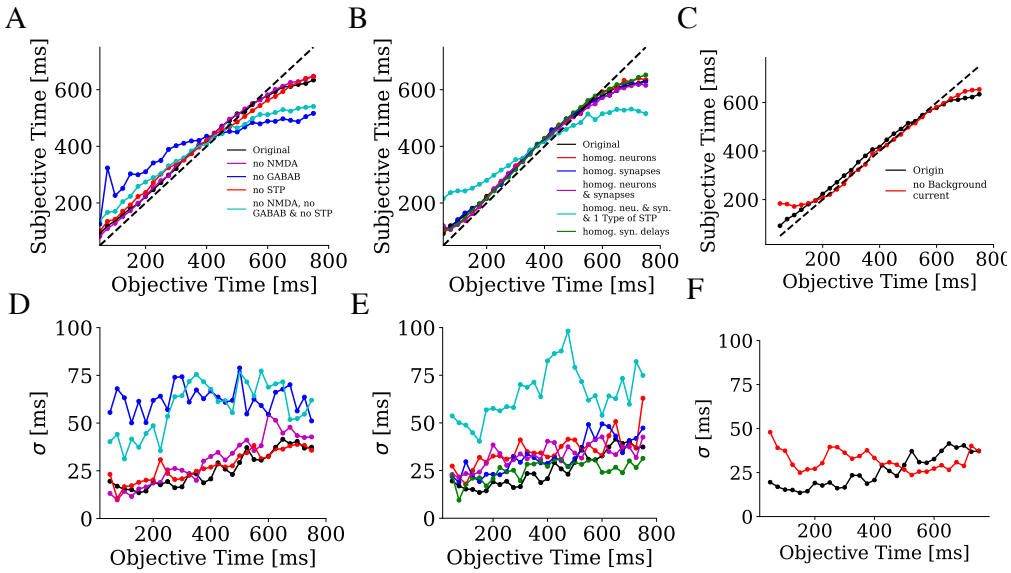

Fig 13. Ablation studies.
Estimated times (panels **A-C**) and standard deviations (panels **D-F**) as a function of test interval durations for different ablation studies. **A, D** Removing of synaptic processes, namely NMDA (magenta curves) and $GABA_B$ (blue curves) currents, short-term plasticity (STP, red curves) and the combination of all three (cyan curves). **B, E** Removing the heterogeneity of the neuronal parameters (red curves), of the synaptic parameters (blue curves) and of both (magenta curves), additional reduction to one type of STP within each pair of neuron types (light blue curves) and removing the heterogeneity of synaptic delays only (green curves). **C, F** Removing of the background current within the PFC model (red curves). In all panels, the original results from Fig. 2B and C are re-plotted in black. The corresponding fitting error values and fit parameters are shown in Table 5 and 6.

Regarding synaptic dynamics, there are three elements with long time constants which might influence the estimation of time: NMDA currents, $GABA_B$ currents and short-term plasticity (STP) of each of the synaptic currents. In order to test their specific influence in time estimation, we conducted ablation experiments by removing each of these synaptic processes, adjusting the background current and synaptic weights to compensate for missing inputs and retraining the readout layer. The resulting fitting errors $RMSE_t$ for the linear psychophysical law and the parameters of Vierordt's law (slope and indifference point IP) are reported in Table 5, while the parameters related to Weber's law, such as $RMSE_{pl}$ and the fit parameters for the piecewise linear fit are presented in Table 6.

Removing NMDA synapses and STP had no effect on estimated times, see Fig. 13A and B in magenta and red, Table 5 and Table 6. In contrast, if $GABA_B$ is removed, such that inhibition is limited to $GABA_A$ with much faster time constants, time estimation is worse, reflected in higher $RMSE_t$ values and a much more pronounced Vierordt's law, see Table 5 and Fig. 13A in blue. Furthermore, the linear fitting error of the standard deviations $RMSE_{pl}$ is higher, see Table 6. To test the combined effect of $GABA_B$, STP and NMDA, we removed all three of them in a further simulation, yielding a slightly lower $RMSE_t$ value compared to ablating $GABA_B$ alone, but a higher $RMSE_{pl}$ value.

As a next step, we tested the role of the heterogeneity in neuron and synapse

Table 5. Ablation studies to identify the components of linear timing

Ablation	$RMSE_t$ [ms]	Slopes	Two sample t-test of slopes to original	IP [ms]
original	49.3 ± 10.5	0.83 ± 0.05		530.0
Synaptic mechanisms				
no NMDA	48.0 ± 13.7	0.85 ± 0.06	$t(98)=2.21$, $p < 0.03$	563.7
no $GABA_B$	140.6 ± 18.2	0.42 ± 0.09	$t(98)=-28.03$, $p < 0.001$	447.0
no STP	53.3 ± 12.32	0.79 ± 0.06	$t(98)=-3.58$, $p < 0.001$	469.2
no NMDA & no $GABA_B$ & no STP	106.3 ± 18.1	0.59 ± 0.08	$t(98)=-16.65$, $p < 0.001$	444.2
Heterogeneity				
homogen. neurons	50.9 ± 15.4	0.86 ± 0.05	$t(98)=2.93$, $p < 0.005$	570.7
homogen. synapses	54.2 ± 13.2	0.82 ± 0.05	$t(98)=-0.64$, $p = 0.52$	546.6
homogen. neurons & synapses	54.2 ± 16.4	0.82 ± 0.06	$t(98)=-0.99$, $p = 0.32$	525.3
homogen. neurons, syn., 1 type of STP	122.2 ± 24.6	0.51 ± 0.09	$t(98)=-21.29$, $p < 0.001$	446.9
homog. syn. delays	44.0 ± 8.6	0.86 ± 0.04	$t(98)=3.61$, $p < 0.001$	586.8
Irregular background activity				
no background current	55.4 ± 10.6	0.81 ± 0.05	$t(98)=-25.39$, $p < 0.001$	220.9

parameters. In the original simulations, these parameters are randomly drawn from distributions that are specific for each neuron and synapse type [46]. Here, we use homgeneous parameters within each neuron type. To this end, we first removed the heterogeneity within each neuron type for the neuronal parameters, second, for the synaptic parameters connecting each pair of neuron types and finally for both parameter sets. For all three cases, fitting errors $RMSE_t$ and $RMSE_{pl}$ are slightly higher compared to the original case (see Table 5 and Table 6). When then further reduce heterogeneity by using only a single type of STP for each pair of neuron types (see Methods for details). This manipulation resulted in higher fitting errors $RMSE_t$ and $RMSE_{pl}$, a much more pronounced Vierordt's law as well as higher standard deviations, see cyan line in Fig. 13B and E and Table 5 and Table 6. Finally, using homogeneous synaptic delays (which are also randomly drawn in the original simulations) for all synapses does not affect timing, see green line in Fig. 13B and E and Table 5 and Table 6.

In order to determine whether the background activation of neurons in between two subsequent stimulations might be responsible for the linear timing results, we removed the background current to all neurons, such that no pronounced activity could be seen between intervals. Removing the background current did not impair timing accuracy

Table 6. Ablation studies to identify the components of Weber's law

Ablation	$RMSE_{pl}$ [ms]	piecewise linear fit a	b	c
original	3.5	0.04	9.8	910.4
Synaptic mechanisms				
no NMDA	3.7	0.06	6.1	625.0
no $GABA_B$	6.7	0.03	56.2	275.0
no STP	3.2	0.03	14.0	691.1
no NMDA, no $GABA_B$ & no STP	7.9	0.11	26.7	341.1
Heterogeneity				
homogen. neurons	5.6	0.03	23.5	812.9
homogen. synapses	4.8	0.04	17.7	958.9
homogen. neurons, synapses	3.8	0.04	20.5	400.1
homogen. neurons, syn., 1 type of STP	9.4	0.08	40.2	400.0
homog. syn. delays	3.1	0.04	14.3	375.0
Irregular background activity				
no background current	5.3	-0.02	37.4	525.0

(Table 5 and Fig. 13C), but disrupted Weber's law with a negative slope near zero (Table 6 and Fig. 13F). Furthermore, we showed before that increasing noise levels up to 1000 Hz yielded larger timing errors and gradually shifted the cut-off value c of the piecewise linear fit of the scalar property towards shorter intervals (see Table 1 and Fig. 7C and D).

Origin of the scalar property

Here, we discuss how the scalar property of the timing errors arises in the state-dependent model. Fig. 14 shows an overview over the proposed mechanism:

1. The network is divided in pools with similar neuronal and synaptic properties among its members, see bottom of Fig. 14A. All pools are activated by the first stimulus and are hindered from firing again by strong inhibitory currents, which are kept active for a long time after the first stimulus is gone by the slow $GABA_B$ component. Due to the considerable heterogeneity of these parameters within the network, the different pools i recover from inhibition at different times, reflected in a firing probability $p_i(t)$ that peaks close to one at a specific time T_i (Fig. 14G). The time course of p_i scales similarly for all pools, e.g., the respective curves $p_i(t/T_i)$ are almost identical for the different pools if time t is scaled by T_i.

2. Each pool consists of N_i neurons, each with firing probability $p_i(t)$ at a given time t. If each neuron is assumed to fire not more than one spike in response to the second stimulus (which is true for the vast majority of neurons within the pools), the relation between the mean and standard deviation of the firing rate FR_i (i.e., number of firing neurons) at the time of the second stimulus is determined by the binomial distribution (Fig. 14H).

3. The firing rates of the different pools are translated into tuning curves O_j of the different output neurons j by convolving the rates with a kernel of synaptic weights that takes the form of a relatively homogeneous *temporal receptive field*

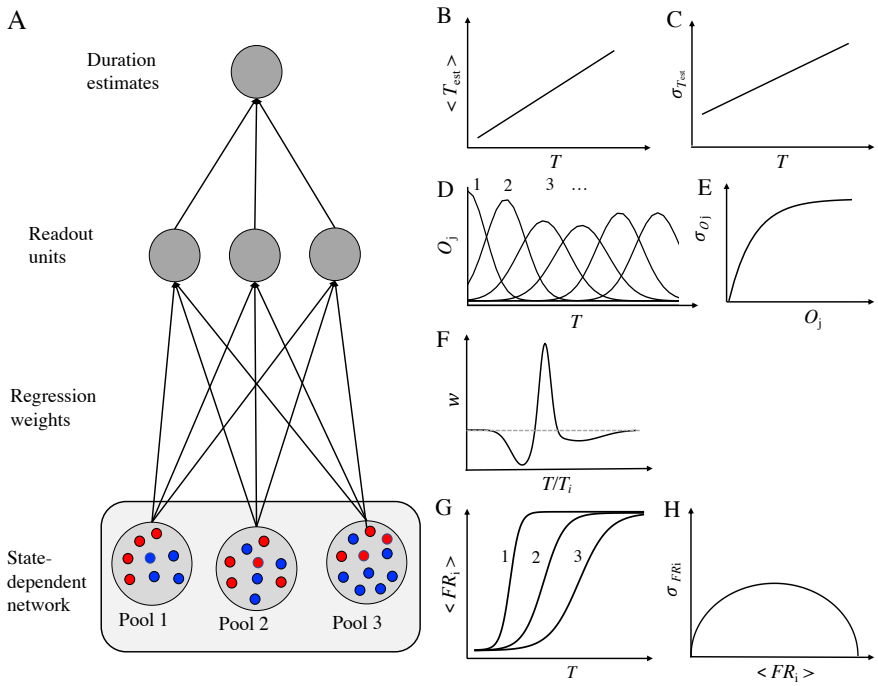

Fig 14. Overview on the derivation of the scalar property
A Translating the activity within interval-sensitive pools (bottom, blue: excitatory and red: inhibitory) into timing estimates and their standard deviations (top). **B,C** Multiplying the readout units with their corresponding time duration and summing up over all readout units leads to the estimated times and the scalar property. **D** Tuning curve-shaped outputs are generated within the readout neurons with a defined relation between mean and standard deviation (panel **E**). **F** Synaptic weights from the pools to the output neurons, forming a stereotype *temporal receptive field*. **G** Firing probabilities peaking at one close to the encoded time of each of the pools. **H** Relation of mean and standard deviations of the firing rates, following from the binomial distribution.

(Fig. 14F). Thus, all output neuron activities O_j show a similar relation between their mean and their standard deviation (Fig. 14E), similar to the firing rates FR_i of the pools in the network.

4. Finally, the activity O_j of each output neuron (Fig. 14D) is multiplied with the interval duration T_j that neuron represents and summed up to form the estimate of the interval duration between the two stimuli (Fig. 14B). As only a few output neurons with similar represented durations T_j contribute to this estimate, the standard deviation of the estimate scales approximately linear with its mean (Fig. 14C), which is the scalar property.

In the following, we elaborate on each of the above steps in reverse order, starting with the end result, the scalar property, and relating each of the assumptions of the mechanism outlined above to observations in the simulations. Regarding step 4 (the scalar property resulting from uniform tuning curves of the tuning curves, Fig. 14B-E), Fig. 16A shows the relation between the mean and the standard deviation of the activity of each of the output neurons O_j (cf. lines and shaded areas in Fig. 2A). This relation can be well-fitted to the function $\sigma_{O_j} = \sqrt{c_j < O_j >}$ with a relatively constant c_j across output neurons j (0.26 ± 0.04). As the duration estimate $T_{\text{est}}(t)$ is formed by summing over the activities O_j of each output neurons multiplied by the duration T_j

that neuron represents, mean and standard deviation of the estimate are given by $< T_{\text{est}}(t) >= \sum_j T_j < O_j > (t)$ and $\sigma_{T_{\text{est}}(t)} = \sqrt{\sum_j T_j^2 \sigma_{O_j}^2(t)}$, respectively.

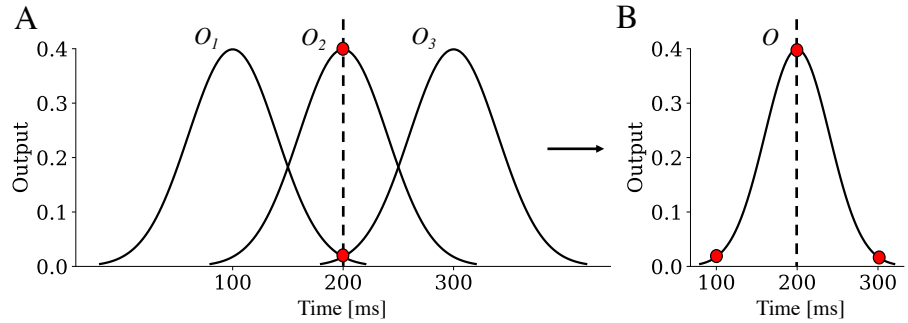

Fig 15. Interpreting the tuning curves of the output neurons as a probability density function
A Illustration of multiple tuning curves (mean-shifted Gaussians with constant standard deviations) evaluated at a given time $t*$. **B** The values of the different tuning curves O_j can be interpreted as the values of a single Gaussian O (centered at $t*$) at different times that correspond to the shifted means. Note that the area under this Gaussian is one, so $O(t)$ can be interpreted as a probability distribution function for the time t elapsed relative to $t*$.

Assume that we want to compute both quantities at a given time t^*. Under the assumption that all tuning curves $< O_j >$ have the same shape, namely mean-shifted Gaussians with constant standard deviations (Fig. 15A), we can interpret the values $< O_j(t^*) >$ of the different output functions j at this time t^* as the values of a single function $< O(t) >$ at different times t that reflect the shift of the mean of each of the different Gaussians (Fig. 15B). Given the fact that the output activities are normalized such that $\sum_j < O_j(t) >= 1$ for all times t, we can interpret $< O(t) >$ as the probability distribution of the time t elapsed relative to t^*. Thus, the average of elapsed time with respect to $< O(t) >$ (or $< O_j(t^*) >$, equivalently) is t^* and we can write

$$< T_{\text{est}}(t^*) >= \sum_j T_j < O_j(t^*) > =< t >= t^* \tag{2}$$

and, using $\sigma_{O_j} = \sqrt{c < O_j >}$ (see above) and $\text{Var}(t) =< t^2 > - < t >^2$,

$$\sigma_{T_{\text{est}}(t^*)} = \sqrt{\sum_j T_j^2 \sigma_{O_j}^2(t^*)} = \sqrt{c \sum_j T_j^2 < O_j > (t^*)} = \sqrt{c}\sqrt{< t^2 >} \tag{3}$$

$$\sqrt{c}\sqrt{< t^2 >} = \sqrt{c}\sqrt{\text{Var}(t) + < t >^2} = \sqrt{c}\sqrt{\text{Var}(t) + < t^* >^2}. \tag{4}$$

$\text{Var}(t)$ is a constant that reflects the width of the tuning curves (about 25 ms for the almost constant curves representing interval durations up to 300 ms) while $\sqrt{c}$ is the Weber fraction.

Together, eqn. 2, 3 and 4 yield the generalized Weber law [4]

$$\sigma_{T_{\text{est}}(t^*)} = \sqrt{c}\sqrt{\text{Var}(t) + < T_{\text{est}}(t^*) >^2} \tag{5}$$

In the generalized Weber law, a constant error dominates the standard deviations of the timing estimates from short durations, resulting in a decreasing Weber fraction, until the linear part dominates for longer intervals and the Weber fraction becomes

constant. Indeed, the state-dependent PFC model shows this often-observed behavior of the Weber fraction (Fig. 2D).

We test the accuracy of the above calculations by computing the Weber fraction $\sqrt{c}$ from the data in two ways: First, as the ratio between the standard deviations $\sigma_{T_{\text{est}}(t^*)}$ and the means $< T_{\text{est}}(t^*) >$, which yields $\sqrt{c}$ for long enough intervals (see above). And second, as the square root of the sum of the variances in all output neurons O_j. This second relation, $\sqrt{c} = \sum_j \sigma_{O_j}$ follows from the normalization $\sum_j < O_j(t) >= 1$ in combination with $\sigma_{O_j} = \sqrt{c < O_j >}$. Indeed, the results of two calculations are in good agreement to each other (Fig. 16B), except for the expected deviations for short intervals.

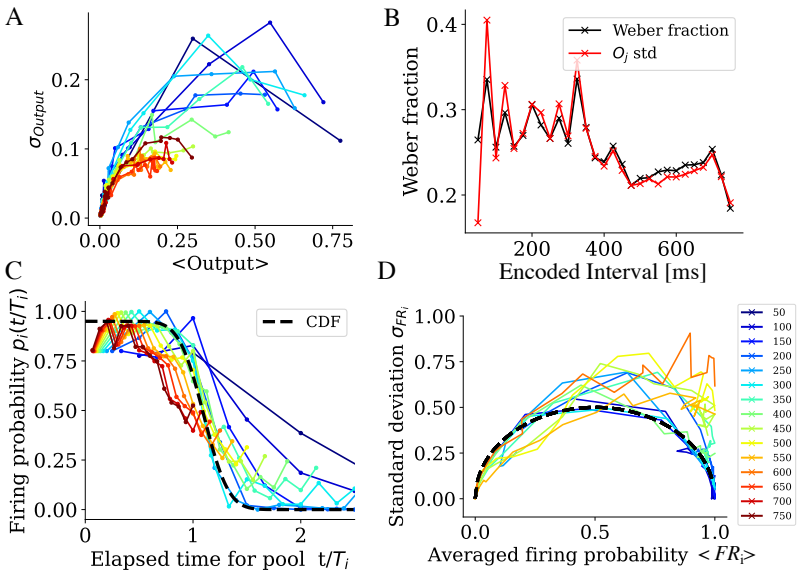

Fig 16. Assessing the origin of the scalar property
A. Standard deviations of the output neuron activity as a function of their mean activity. See panel D for the color code. **B.** Weber fractions (black curve, standard deviation of the duration estimated divided by its mean) and square root of the sum of the variances of all output neurons (red curve) for each of the encoded interval durations. **C.** Firing probability of each pool i as a function of time, scaled by the duration T_i that is represented in that pool. See panel D for the color code. The dotted line shows the best fit of a normal cumulative distribution function (CDF) to all curves. **D** Standard deviation of the firing probabilities as a function of the mean shown in panel C. Apart from pools encoding long durations, the curves are well-fitted by the relation predicted by the binomial distribution (dotted line). The colors correspond to the intervals that are represented in each pool (see color bar, cf. Fig. 2A).

Regarding step 3 (uniform tuning curves of the output neurons resulting from uniform firing rate and weight profiles, Fig. 14D, F and G), we have seen in Fig. 8B and D that both firing rates and readout weights follow highly stereotype temporal profiles for each pool i when time is scaled to the duration T_i that is represented in that pool. The firing rates (or, more precisely, the firing probabilities p_i) can be well described by a cumulative normal distribution (Fig. 16C, where p_i is plotted for a given time t as a function of the represented time T_i for all pools) and the weights follow an asymmetric version of the Mexican hat function (Fig. 8B, black line). The symmetric Mexican hat is a well-known synaptic profile in spatial processing in the visual system [58, 88]. Here, the asymmetric version accounts for the different slopes of firing rate distribution before

and after the interval that is represented in the corresponding output neuron (Fig. 16C).

Regarding step 2 (firing probabilities following a binomial distribution, Fig. 14H), recall that the binomial distribution describes the number of successes (here: spikes) in a sequence of N random experiments (here: neurons), where each success has the same probability p. Thus, the binomial distribution can be used to estimate the firing rate in a pool with N_i neurons and $p_i(t)$ at time t (we will abbreviate $p_i(t)$ with p_i in the following when the particular time t does not need to be emphasized). In particular, the mean firing rate $< FR_i >= N_i p_i$ of the pool i and its standard deviation $\sigma_{FR_i} = \sqrt{N_i p_i (1 - p_i)} = \sqrt{N_i (p_i - p_i^2)}$ are known from this distribution. For small to moderate p_i, σ_{FR_i} can be approximated by $\sqrt{N_i p_i}$, neglecting p_i^2. This approximation was already used in step 4 when fitting the standard deviations of the output neuron activities (Fig. 14E and Fig. 16A).

Fig. 16D shows the relation between mean and standard deviation of the firing probabilities p_i of each pool. p_i is estimated by normalizing the mean firing rates FR_i to the maximal value in each pool. The standard deviation is fitted to the relation from the binomial distribution $\sigma_{FR_i} = \sqrt{N_i p_i (1 - p_i)}$ and the values in the figure are divided by the fit parameter $\sqrt{N_i}$. The fit is good for pools representing short intervals, but gets worse for $T_i > 400$ ms. The estimated N_i values from the fit match the actual pool sizes well (estimate from the fit to the binomial distribution: 16 ± 5, average actual pool size: 14 ± 5) with no statistical difference (two sample t-test: $t(28) = 0.936$, $p = 0.36$).

Regarding step 1 (stereotype firing rate profiles in the different pools of the network, Fig. 14G), the cumulative normal distribution of the firing rates (Fig. 16C) follows from the fact that each neuron fires as soon as its particular firing threshold is crossed. Given that the membrane potential of each neuron is driven by noise that can be approximated by a normal distribution, the probability to cross the threshold at a given time is the cumulative normal distribution with the difference of the mean membrane potential $< V_i(t) >$ from the threshold $V_{th,i}$ as the mean. The standard deviation of the membrane potential does not systematically change over time, as neurons are driven back toward their resting potential by leak currents, which can be described by the Ornstein-Uhlenbeck process [93] for which the standard deviation is constant in time. Thus, the change in $p_i(t)$ over time is mainly driven by changes in the mean membrane potential $< V_i(t) >$. The main driver of this change over time is the slow $\mathrm{GABA_B}$ inhibition after the first stimulus, which effectively prevents neurons from firing in response to a second stimulus within a certain window of time. Apart from the time constant of the $\mathrm{GABA_B}$ conductance, this time window is determined by the neuronal and synaptic parameters within each pool. As we have seen in Fig. 11, the mean current difference to the neurons' rheobase increases for pools encoding longer intervals (which can be translated into the difference between the average membrane potential and the firing threshold). Thus, more of the inhibition from the first stimulus must be worn off before those pools can respond to the second stimulus, so that happens at later times. In summary, the increase of p_i over time is mainly due to a gradual decay of long-term inhibition which decreases the difference between average membrane potential and firing threshold and thus, increases the chance of each neuron to fire. The different parameters in each pool determine the speed by which p_i increases over time.

To verify that the observed scaling of p_i can be reproduced by the mechanism described above, we have constructed a minimal model simulating a single neuron that receives a large amount of random, balanced excitatory and inhibitory currents and is subject to a $\mathrm{GABA_B}$ current following the time of the first stimulus and to a fixed depolarization at the time of the second stimulus (see Methods for details). Simulating this neuron of a large number of trials allows to estimate p_i for a given firing threshold $V_{th,i}$. For simplicity, we simulate the different pools by varying $V_{th,i}$, although the above results suggest a variation of the synaptic properties. For each simulated pool i,

we compute the first time T_i at with p_i exceeds 95% and record T_i as the represented duration of this pool. When time is scaled by this duration $p_i(t/T_i)$ shows the same cumulative normal distribution time course for each pool (Fig. 17), as we see in the network model (Fig. 8D).

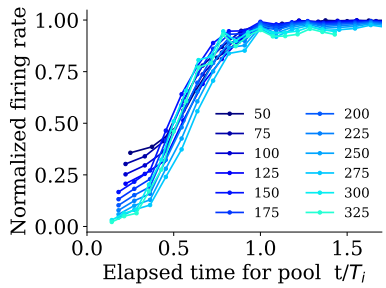

Fig 17. Results from the minimal model.
Normalized firing rate as a function of simulated time, shown as a fraction of the encoded interval duration of each pool (color-coded). Each curve was generated by a different threshold for the membrane potential to elicit a spike. Higher thresholds lead to longer durations that need to elapse before that first spike (cf. Fig. 11). When scaling this time by the duration T_i at which the neuron spikes with 95%, the firing rate curves for all durations largely overlap, as in Fig. 8D for the full model.

Overall, each step of the theory outlined above can be supported by results from the full model, so it can be seen as a plausible explanation for the occurance of the scalar property in the state-dependent PFC model.

Deviations from the scalar property and the origin on Vierordt's law

The theory of the scalar property derived above rests on a number of assumptions. First, firing rate curves and weight kernels need to be roughly the same for all pools after scaling time with the duration each pool represents (Fig. 8B and D). Second, output activations must be small enough such that the standard deviation can be approximated by the square root of the mean (Fig. 16A). And finally, the output tuning curves need to have the same shape for all output neurons. While the first two assumptions are met, it is apparent from Fig. 2A the third assumption is violated for output neurons representing intervals that are longer than 350 ms, where the tuning curves quickly grow broader as intervals durations increase. Here, we discuss consequences of violating the assumption of stereotype tuning curves of the output neurons.

If we consider the most extreme case where all curves O_j are completely flat such that all intervals contributes to the estimate with the same weight, it follows from the normalization of $O_j(t)$ to one that for each time t^*, the same duration estimate $< T_{\text{est}} >$ is generated independent of the real time t^*, which is the average over all represented intervals T_j. As the standard deviations are linked to the mean duration estimate, the standard deviations are also constant in time in this case. In intermediate cases, combining constant, sharp tuning curves O_j for short intervals T_j and increasingly broader curves for longer intervals, the scaling of both the mean and standard deviation are shifted away from the linear relations described in Eq. 2 and 5 and towards constants values. This implies that deviations from the scalar property and Vierordt's law, the observation that long intervals are underestimated and short ones are overestimated, are mechanistically linked.

Indeed, for most manipulations described above, a positive linear relation can be found between the slope of Vierordt's law (where a slope of one corresponds to a

one-to-one relation between subjective and objective duration and a slope of zero to a constant estimate for each duration) and the point in time where Weber's law saturated into a constant value - the closer the slope is to one, the broader the range of intervals for which the scalar property holds (Fig. 18A, $r = 0.75, t(12) = 5.93, p < 0.01$). Furthermore, a strong negative linear relation is found between the slope of Vierordt's law and the minimal standard deviation of the output curves O_j, see Fig. 18B ($r = -0.96, t(12) = -11.88, p < 0.01$).

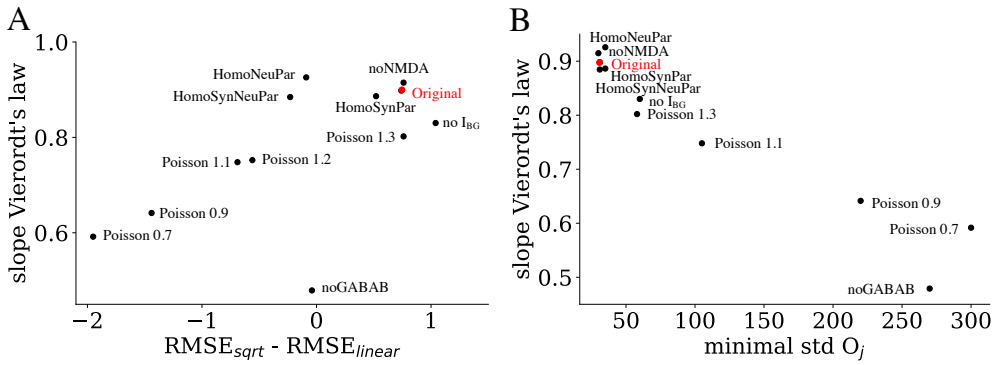

Fig 18. Relation between Vierordt's law and the scalar property.
A. Calculating the difference of $\mathrm{RMSE_s}$ - $\mathrm{RMSE_l}$ and comparing against the slope of Vierordt's law shows a linear trend for different ablation studies and varying Poisson noise. The higher and positive the difference, the stronger the slope of Vierordt's law and the stronger the evidence for scalar property except for the ablation of $\mathrm{GABA_B}$.
B. Comparing the minimal standard deviation of the output curves O_j against the slope of Vierordt's law for the different cases, results in a strong negative linear trend. The smaller the standard deviation, the better the estimation.

Ruling out alternative mechanisms

Having found a suitable mechanism for time perception in compliance with the experimental results, we checked whether other possible mechanisms could explain timing within the state-dependent PFC model. First, we tested whether the neurons encoding a specific pool show a ramping activity over time, cf. Fig. 19A to rule out the timing model proposed by Durstewitz [20]. We calculated the trial averaged firing rate of each neuron step wise in 10 ms bins for all test intervals (color-coded). An increase of the firing rate over time, which maximizes at the corresponding timing interval could not be seen here, see Fig. 19A.

Lastly, we tested whether there is sequential activation of subsequent pools analogous to a synfire chain [44]. To this end, Fig 19B shows the normalized fraction of synaptic weights from one pool to another. This fraction is relatively small compared to the overall synaptic weight onto the neurons (Fig. 19C) and specifically, no sequential activation of pools could be seen in the pool-to-cool connectivity matrix in Fig. 19C, Thus, we can discard the idea of a sequential activation of the pools.

Discussion

We investigated whether the established state-dependent network model of time perception [13] still works when embedded into a strongly data-driven network model of the prefrontal cortex [46] and whether it is able to reproduce some of the most

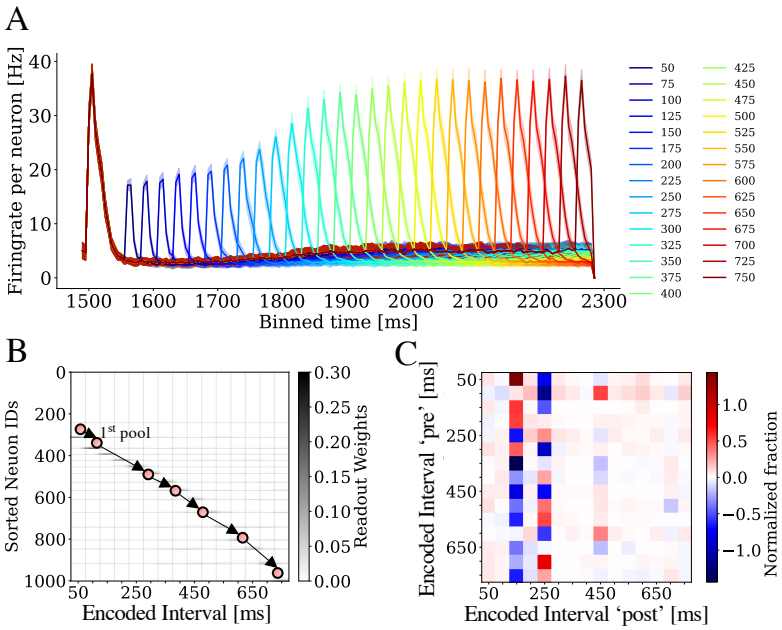

Fig 19. Ruling out alternative mechanisms.
A. Averaged binned firing rate (binning interval of 10 ms) in each interval-encoding pool (color-coded) as a function of binned simulation time to test for ramping activity. Shaded region indicate the standard deviation over 50 trials. **B.** Illustration of a hypothetical sequential activation of interval-encoding pools. **C**. The averaged synaptic weights from each pre-synaptic pool (rows) to each postsynaptic pool (columns), normalized by the overall input to each pool.

important experimental results on time perception, namely the linear psychophysical law [24], the scalar property or Webers law [31] and the modulation of subjective duration by dopamine [11]. Indeed, the model can successfully reproduce the psychophysical law and Webers law for intervals in the range of 50 - 750 ms. The modulation of the D2 dopamine receptor was tested by modifying neuronal and synaptic parameters and yielded, within a smaller range of 200 - 600 ms, the expected slowing of the internal clock for an antagonistic modulation (up to $-50\,\%$) and, conversely, the speeding of the internal clock for an agonistic modulation (up to $20\,\%$). In the following, we discuss the dynamic mechanism underlying time perception in this model, as well as the implications of the present work for explaining the three above-mentioned experimental results. Finally, we relate the current model to other models on time perception.

Mechanism and limitations of time perception within the state-dependent PFC model

We found that different interval durations are encoded in specific populations of neurons that were identified by the readout neuron onto which each neuron projects with the largest synaptic weight. Each duration-specific neuron pool shows a stereotypic firing rate response to the second stimulus that gradually increases as the interval becomes longer, up to a maximum just before the interval duration the pool encoded, and for all longer intervals as well (Fig. 8D). These curves are reminiscent of the psychometric response curves that are seen in many common time perception paradigms, e.g., [65]. Importantly, the curves show very similar profiles when the time elapsed is scaled to the duration each pool represents (Fig. 8D). This similarity allows the readout neurons to

decode elapsed time from the firing rate of the neurons (the "states") of the network at a given time. The scale invariance in the response of the pools is also an important prerequisite for the scalar property of timing errors, as we discuss in more detail below.

As we illustrate using a minimal model, the stereotypic response can be reproduced by a single neuron that is subject to random synaptic input and slow inhibition. For a given mean and standard deviation of the input, the firing of the neuron is governed by the binomial distribution. If the mean of the synaptic input increases over time, the firing rate approximates a cumulative normal distribution (Fig. 17). The scaling of this distribution is determined by the distance of the mean input current from the neuron's rheobase, relative to its standard deviation. Thus, two ingredients are needed to explain the shape of the firing rate curves (and thus, the ability of the model to encode durations within a certain range): A synaptic current that systematically changes over time and a substantial variation of neuronal and synaptic parameters between different neurons (or pools of neurons) encoding different interval durations.

Regarding the full network model, we conducted a series of correlation and ablation studies to identify the source of these two factors. First of all, we found that both the distance of the average membrane potential from the threshold (Fig. 9B) and the distance of the average current from the rheobase (Fig. 11B) increases for pools encoding longer intervals, consistent with the theory derived from the minimal model. Regarding the source of the systematic change in the input current, the ablation studies identified the slow $GABA_B$ current as the most important component, as its ablation leads to a much worse fit to the linear psychophysical law, a much more pronounced decrease of its slope in relation to a one-to-one relation (Vierordt's law) and a higher trial-to-trial variability of duration estimates. Ablation of any other synaptic components with long time constants (NMDA and short-term plasticity, STP) or removal of neuronal or synaptic heterogeneity did not have such an effect (Table 5). On the other hand, removing $GABA_B$ also does not abolish the ability of the model to encode time altogether. So apparently, the synaptic processes with shorter time scales (AMPA and $GABA_A$) can also provide a time code, albeit with less accuracy (larger deviations between subjective and objective duration) and precision (larger standard deviations across trials).

To investigate differences in the neuronal and synaptic parameters of neurons in different pools that may explain their tuning to different intervals, we conducted a linear discriminant analysis (Table 3) and also assessed differences between the pools for each of the parameters found relevant for discrimination. The fact that both excitatory and inhibitory synaptic weights are among the strongest determinants of the discrimination function and also significantly increase for pools encoding longer durations (Fig. 12D) agrees with the observation that excitatory and inhibitory currents show the same behavior (Fig. 10C-E). Interestingly, the overall current does not change significantly between pools, nor the rheobase of the pool members (Fig. 11), but only the difference of the total current onto each neuron minus the rheobase of that neuron does (Fig. 11B). So averaged across the neurons within a pools, excitatory and inhibitory currents remain balanced, producing irregular activity [94], while the current onto each neuron maintains a specific distance to its respective rheobase, allowing selectivity of each pool for a specific interval. This may also explain why the rheobase contributes to the discrimination between pools together with the synaptic weights, while it does not significantly differ between pools on its own. Regarding synaptic connectivity, the number of inhibitory connections discriminates between interval-selective pools, while the number of excitatory connections does not. This finding further emphasizes the role of GABA, especially $GABA_B$, for time perception. By the same token, both STP time constants of inhibitory synapses discriminate between intervals and overall, STP systematically shifts towards synaptic facilitation for pools encoding longer intervals

(Fig. 12B and C). Finally, the membrane time constants as well as the synaptic delays of excitatory synapses also increase for pools encoding longer intervals, consistent with the observation that the peak membrane potential after the first stimulus is reached at later times for pools encoding longer intervals (Fig. 9C). However, as all of these differences only amount to a couple of milliseconds, it is unlikely that these observations are of functional relevance for time perception in the range of hundreds of milliseconds.

Given the importance of parameter differences between the different pools for encoding different interval durations, we expected to see an impairment of time perception when removing heterogeneity in the neuronal or the synaptic parameters or both. Interestingly, this was not the case - neither accuracy (Fig. 13B) nor precision (Fig. 13C) of time perception was impaired by this manipulation. Note that even if the variability of each parameter was set to zero by replacing the respective distribution of values by the mean value, there is still heterogeneity left by means of the different types of neurons (pyramidal cells and four types of interneurons in two layers, see Methods for details), connection probabilities and STP types (facilitating, depressing and a combination of both, each expressed with a different probability for each combination of pre- and postsynaptic neuron types). Indeed, if we reduce the heterogeneity of the STP types, timing strongly impaired (Fig. 13B and D, cyan curve).

We also assessed potential limitations of the model in terms of the length of the intervals that can be encoded and the levels of noise that can be tolerated. Already within the range of tested interval durations, we observed deviations both from the one-to-one psychophysical law (Fig. 2B) and the scalar property (Fig. 3) at interval durations above 500 ms. Both effects are even more pronounced when the network is trained for longer intervals, up to 2000 ms. Indeed, Fig. 7A and B suggest that there are two distinct linear regimes both for the psychophysical law and the scalar property for intervals above and below 500 ms, respectively. Finally, we observed a gradual broadening of the tuning curves of the readout neurons for intervals above 300 ms (Fig. 2A). Given the importance of $GABA_B$ for precise and accurate time perception, it stands to reason that these limitations are connected with the time constants of $GABA_B$. Indeed, the rise and decay time of that current add up to 300 ms, the interval duration where the tuning curves begin to degrade.

The gradual decrease in timing accuracy with increasing noise levels (Fig. 7C) as well as the deviation from the scalar property (Fig. 7D) can be explained in a similar way: As the levels of external noise increase, each output neuron becomes less predictive of the interval duration it represents, resulting in broader and shallower tuning curves, which are linked to both phenomena illustrated in Fig. 7C and D.

Implications for experimental results on time perception

Linear psychophysical law

The linear relation between subjective and objective time is among the most robust psychophysical findings in time perception [24] and thus, its fulfillment is seen as an important criterion for model validity. In the state-dependent PFC model, the stereotype firing rate profiles relative to the criterion time in each of the interval-sensitive pools of neurons form the neuronal basis for the linear psychophysical law. By extension, each of the readout neurons show a similar tuning curve in response to the second stimulus and thus, even stimuli that are presented at durations that are not explicitly trained for can be represented, as the (similar) tuning curves of the readout neurons encoding intervals nearby can provide a suitable interpolation. Small deviations from linearity can be seen at very short and very long durations (compare dash-dotted line to data in Fig. 2B), resulting from boundary effects (incomplete tuning curves, see Fig. 2A, dark blue and dark red curves). Independent of these effects, a

decrease of the linear slope of the psychophysical law compared to one and thus, an overestimation of shorter and an underestimation of longer intervals (Vierordts law [33, 96]), can also be observed in the model. We showed that under the assumption of moderate, perfectly constant standard deviations of the tuning curves for all interval-selective output neurons, an exact one-to-one relation between subjective and objective time follows. Vierordt's law occurs if the standard deviations of the tuning curves increase for output neurons encoding increasing interval durations. This is the case for intervals exceeding the dominant time scale of the model, the combined rise and decay time of the $GABA_B$ current, but also if this current is removed at all or increasing levels of external synaptic noise are added.

Previous studies have attempted to explain Vierordt's law in a Bayesian framework, where current temporal information is combined with expectations from previous trials [33, 79]. A recent study analyzed the results from the classic experiments of Vierordt within such a framework [33] and found that much of the deviation from a one-to-one relation between subjective and objective time can be attributed to the specific experimental protocol used in these studies, namely a completely random variation of interval durations between trials. Within the Bayesian framework, a more naturalistic, gradual change of durations (using a random walk) abolished the distortion. Interestingly, when the authors performed a new experiment comparing both protocols, they found a residual distortion even in the random walk condition. The slope of the resulting psychophysical law was about 0.86, which is remarkably close to the slope we report for the current model without any ablations (0.83, Table 5). Thus, it seems likely that Vierordt's law arises as a combination of Bayesian integration of information from previous trials and a distortion that is intrinsic to the network that generates the current duration estimate.

Regarding the indifference point, the duration at which subjective and objective duration coincide despite a slope smaller than one, we found a relatively constant value around 500 ms for all of the different parameter sets as long as the same range of intervals (50 ms to 750 ms) is used for training the weights of the readout network. This value differs significantly from the arithmetic mean of all trained intervals (400 ms), which is supported by parts of the experimental literature [64, 101, 103], but not others [6, 28, 64]. However, the indifference point does increase when a larger range of intervals has been used for training (50 ms to 2000 ms), suggesting that the indifference point can be shifted by training.

The scalar property

The scalar property, or Weber's law, the linear increase of the standard deviations of timing estimates with the mean duration that is estimated, is an important experimental result that has often been cited as a cornerstone of time perception. Thus, any sensible model of time perception should be able to reproduce the scalar property, at least for a limited range of durations [32].

For the present model, we expected a sublinear instead of a linear scaling of timing errors, as such results were reported in a study on one of its variants [59]. Surprisingly, the scalar property did emerge in our version of the model (Fig. 3), up to durations that correspond to the time constants of the $GABA_B$ current. The importance of this current is underlined by the fact that its ablation leads to a drastic decrease of the cut-off duration where Weber's law is replaced by a constant timing error (Table 6). We also found a plausible explanation for the origin of Weber's law, combining profiles of firing probability that are scaled by the duration represented in each time-specific pool of neurons with a stereotyped temporal receptive field occurring from optimizing the readout from each of the pools in downstream units, both resulting in largely uniform shapes of temporal tuning curves in these output neurons and finally, constant Weber

fractions. In this regard, the mechanism generating Weber's law bears similarity to the scalar filter banks in Grossberg's spectral timing theory [38] and also to the multiple synfire chains in [44], each of which accounting for a given time interval and contributing to a timing error that scales approximately linearly within a certain range of durations. In contrast to these studies, however, the pools of neurons that represent specific durations arise spontaneously from the heterogeneity in the synaptic parameters, rather than being imprinted into the model architecture.

Several previous studies have attempted to explain the emergence of Weber's law from general mathematical principles. Hass and Herrmann [43] have developed an information-theoretical framework to characterize the ability of a given model to reproduce the scalar property. They suggest that the sublinear (instead of linear) scaling of timing errors seen in many models may be caused by a common set of timing mechanisms that are based on the systematic change of some observable quantity in time, such as the firing rate of a neuron or spike in a specific neuron at a given time. The scalar property, on the other hand, is thought to emerge in models that use the increase of standard deviations itself (in a diffusion sense) to estimate time. The latter category comprises models that rely on purely stochastic transitions between neural states [3, 26, 87]. For instance, Simen et al. [87] describe the slow ramping of firing rates by a specific form of drift-diffusion process that is driven by state transitions following a Poisson distribution. The scalar property then follows from the fact that the time between two Poisson-distributed events follows an exponential distribution, which has a constant coefficient of variation (equivalent to the Weber fraction) of one. In the state-dependent PFC model, timing does not turn out to be driven by purely stochastic forces, but by a systematic change in excitability that is mainly driven by the time constant of the $GABA_B$ current. Thus, it can not be classified as a variance-driven model in terms of Hass and Herrmann [43]. Rather, the scalar property is generated by the fact that mean and standard deviation of timing estimates always covary in a specific way, governed by the binomial distribution. One could characterize the state-dependent model as a covert mean-driven model, as the systematic change does not occur in a directly observable quantity.

Note that the deviation from Weber's law at longer intervals takes the form of a timing error that is constant in time (Fig. 3). This kind of deviation is only rarely observed in experiments [35], while a more common observation is a steeper, superlinear increase of the error over time [32, 35]. A possible explanation for this discrepancy may be the fact that we only examined a single mechanism of time perception at a time. In the real brain, it is likely that several different of these mechanisms coexist, potentially each with its own optimal time scale [42]. For instance, it has been shown that the mechanism of ramping activity [20] can represent durations up to several seconds. If this mechanism coexists with the state-dependent mechanism we investigated here, it is likely that the overall time estimate is taken over by ramping activity at intervals that are too long to be represented by the state-dependent network. Under this assumption, the constant timing error predicted for longer durations is not seen because for those intervals, another, more suitable mechanism takes over. Theoretical frameworks for the integration of different sources of time estimates have been proposed earlier [86], including our own proposal of a "temporal hub", potentially located within the basal ganglia [42, 45]. Assessing how the combination of timing mechanisms with different time scales in such a hub would affect the scaling of timing errors seems to be an important direction for future research.

Finally, we note that the deviation from Weber's law and the deviation of the slope of the psychophysical law from one (Vierordt's law) are based on the same mechanism, at least in this model. Regarding experimental studies, this connection suggests that it may be worthwhile to study both laws together when searching for transitions between

different mechanisms of timing or ablating specific neuronal of synaptic mechanisms in real neural systems.

Dopaminergic modulation

The third major experimental result we aimed to reproduce in this study was the modulation of subjective duration by dopamine. We modelled the effects of the D2 dopamine receptor on synaptic and neuronal properties based on results from *in vitro* experiments and, indeed, found that subjective duration is lengthened by D2 activation and shortened by D2 inactivation (Fig. 4), as it has been consistently seen in experiments [11, 83, 91]. As shown in Fig. 4B, the change in subjective duration is mostly driven by the modulation of the synaptic parameters, namely a 20 % decrease in NMDA and a 50 % decrease in GABA peak conductances at 100 % D2 activation compared to 0 % (see Methods for details). As GABA is decreased much more compared to NMDA, D2 activation results in a net decrease of excitability of the network. As time is encoded by means of the firing rates in each of the pools in response to the second stimulus (Fig. 8D), decreased excitability implies that any given firing rate will be reached at a later time under D2 activation and thus, subjective duration will be longer than objective duration. The opposite is true for D2 inactivation.

Understanding this mechanism of the dopaminergic modulation of time perception also helps to explain how the model reproduces a number of effects that are also seen in experiments. First, the scalar property is unaffected by mild D2 modulation (Fig. 5), consistent with experimental results [104]. As D2 activation (or inactivation) simply changes the excitability of the entire network, the neurons in each pool are simply shifted towards later (or earlier) responses, while the relation between means and standard deviations of firing rates that causes the scalar property remains intact. Second, retraining of the output neurons fully compensates the D2 modulation (Fig. 6). This is consistent with experimental findings on chronic application of dopaminergic drugs like methamphetamine to rats [2] and also, more broadly, results suggesting neuroadaptive processes in response to chronic activation of the dopaminergic system, e.g. by addiction [81, 89]. We can explain this effect by a synaptic remapping of neurons within the network that changed their optimal reaction to the second stimulus to earlier or later time under chronic dopaminergic influence: For instance, if neurons in a pool that used to encode 100 ms are sensitive to 150 ms under D2 modulation, a retraining would simply assign them to the output neuron encoding 150 ms. Thus, the change in subjective duration can be fully compensated if the modulation is present long enough such that the synaptic connections to the output neurons can rewire accordingly. This is the case if the D2 activation or deactivation is chronic and stable over time. Finally, we observed limitations both in the interval durations and the D2 activation and deactivation levels within which time perception works properly. In particular, for D2 activations beyond 50 % as well as interval durations shorter than 200 ms, time perception basically stops working. In Suppl. Fig. 1, we see that all time estimates collapse onto a single value for values far beyond these boundaries. D2 deactivation shows similar effects, but subjective durations can still be differentiated for intervals above 200 ms at deactivations of −100 % (Suppl. Fig. 1). Indeed, experimental results using D2 receptor agonists point into the same direction as our findings on D2 receptor activations [104]. More specifically, the study shows that the scalar property breaks down at higher concentrations of the agonist. Within our model, we can explain these results as a boundary effect: Higher D2 concentrations make the entire model overly excitable. Thus, the different pools lose their ability to differentiate between different intervals and timing over a range of intervals is impaired. This proposal is supported by the fact that subjective durations for the different pools collapse onto a single value as D2 activation approaches 100% (Suppl. Fig. 1) and that subjective

durations in pools encoding short intervals (dark blue lines) do so for smaller D2 activation levels, as they are more excitable to begin with.

Note that we have restricted our analysis to the D2 dopamine receptor, as most effects on subjective duration have been reported in relation to this receptor type [11] and it has been shown that the binding affinity of a variety of drugs to the D2 receptor predicts the effect on time perception [71]. Moreover, the effects of D1 receptor activation are likely more complex than a simple change in excitability [21, 63], so we would not expect a systematic change in subjective duration within this model. However, it should be noted that more recent studies did show effects of D1 on time perception as well, in particular in the context ramping activity [77]. Thus, it would be worthwhile to investigate the underlying mechanisms of this modulation as well, and to assess the circumstances under which D1 and D2 modulation is most important, respectively.

Relation to the original state-dependent model

Here, we compare our state-dependent PFC model with the original state-dependent model [13]. The author of the original model showed, using 500 neurons, normalized output peaks up to 250 ms using 50 ms steps for training and peaks up to 400 ms using 100 ms steps. Our time constants for $GABA_B$ are similar, as they have the same rise time $\tau_{rise} = 100\,\text{ms}$, but a slightly longer decay time $\tau_{decay} = 200\,\text{ms}$ (compared to $\tau_{decay} = 166\,\text{ms}$ in [13]). Within the range 50 - 250 ms, we were also able to show similar output patterns, but for longer intervals, our output peaks become broader. Still, our model was able to perform discrimination tasks up to 750 ms. The co-activation of other readout units for longer intervals could also be a biologically possible mechanism to encode time, as there is no identity-shaped time estimation in experiments, rather than an overestimation of shorter intervals and an underestimation of longer intervals, i.e. the Vierordt's law.

Within the original state-dependent model, Buonomano showed reduced timing performance when $GABA_B$ or STP are removed. We were able to confirm the importance of $GABA_B$, but in contrast to the original model, we find that time estimation is still functioning when STP is completely removed. In contrast, reducing heterogeneity of STP by allowing only one type of STP within each given neuron type combination greatly impaired timing performance. To understand this apparent contradiction, note that the prefered STP type for E-to-E connections is facilitating, while for E-to-E connections, it is depressing. Thus, if we limit STP to a single, preferred type for each tpye pf connection type, the network is put into a regime where excitation is facilitated and inhibition is depressed at the same time. This combination will likely make the network overly excitable as whole, impairing the necessary differentiation in excitability between pools. In a recent study of persistent activity within the same PFC network [47], we observed that persistent activity was stabilized when STP was homogenous compared to no STP at all (and also heterogeneous STP, which prevented persistent activity at all). This finding also supports the idea that excitability of the network is enhanced by homogeneous STP, in a similar way as excessively strong D2 receptor activation (see previous section).

Furthermore, Buonomano claimed that temporal tuning was specifically achieved by the variability of the synaptic weights as having zero-varianced synaptic weights did not resulted in interval discrimination. In contrast, when we performed simulations with non-heterogeneous neuronal and synaptic parameters within each combination type (differences between combinations, but equal within a combination), timing could still be encoded. Rather than the synaptic weights, the connectivity might play an even more important role for our timing tasks. Neurons which receive fewer negative inputs from inhibitory neurons can easily be reactivated for a second interval, compared to neurons receiving more inhibitory inputs.

In summary, we propose that in addition to a process with long time constants such as $GABA_B$, most parameters which determine the excitability of a neuron, e.g. membrane threshold, time constants and synaptic weights, are important to assign a neuron into a specific pool. Even if one aspect, for example STP, is removed, there might be other heterogeneous parameters within the network which help to differentiate the neurons to obtain interval discrimination, given sufficient heterogeneity. Furthermore, we note that $GABA_B$ is not the only option for enabling time perception in the range of hundreds of milliseconds. In principle, any process with a sufficiently long time constant could be used, e.g., the influx of Calcium ions following a spike that has already been explored in the context of the ramping activity model [20].

The fact that the state-dependent PFC model showed the scalar property was most surprising, as previous studies on the original state-depedendent network model showed a sublinear rather than a linear scaling of timing errors [59]. We showed that the overall curve of timing errors (averaged over several parameter combinations) is best fitted with a linear part for shorter intervals and a constant part for longer ones (Fig. 3). For any individual parameter combination, the constant part at longer intervals is less clearly visible (e.g. Fig. 2C) and may be mistaken for a decreasing slope in an overall sublinear scaling. Furthermore, we have seen that the saturation of Weber's law into a constant error occurs at durations that are shorter than where linear timing itself is impaired (750 ms compared to 750 ms, Fig. 2B and Fig. 3). Taken together, these results suggest that a reanalysis of the previous data - pooling together different parameter sets and considering a saturation of timing errors at longer intervals - would yield results that are similar to ours.

Conclusion

Computational models provide opportunities to understand the neural mechanisms underlying time perception. We chose a set of key experimental findings to test such models against, namely the psychophysical law (including Vierordt's law), the scalar property of timing errors and the dopaminergic modulation of subjective duration. The state-dependent PFC model is able to reproduce each of these findings for interval durations between 50 and 750 ms, including the scalar property, one of the most enigmatic results in time perception. The model even reproduces several details of the experiments such as the magnitude of the Weber fraction and the slope of Vierordt's law, the dependence of the indifference point upon the range of presented intervals and effect of the D2 dopamine receptor on the scalar property. Remarkably, no explicit tuning of the parameters of the network was necessary to obtain these results, except for the synaptic weights for the readout network. Beyond providing strong support for the present variant of the state-dependent model, these results also strengthen confidence into the underlying network model of the prefrontal cortex [46], which has already shown to reproduce key features of in vivo neural activity without the need for parameter tuning.

The state-dependent PFC model can now be considered the first timing theory that is validated by a range of important experimental results. However, this does not rule out alternative theories at all, especially for interval durations beyond 750 ms. Other prominent approaches such as models of ramping activity [20], synfire chains [44] and the striatal beat model [70, 74] can now be tested in the same way. This will likely lead to a range of validated theories of time perception, and a more thorough understanding how the brain tells time under different circumstances, such as different ranges of durations.

Methods

Network model

To test timing within a realistic prefrontal cortex model, we used the spiking neural network model proposed by [46]. This model can reproduce key features of *in vivo* activity, as the neuronal parameters and synaptic parameters were constrained by anatomical and electrophysiological data from *in vivo* and *in vitro* experiments on rodents. The spiking neural network consists of two laminar components, layer 2/3 and layer 5, of which 47.0 % within layer 2/3 and 38.0 % within layer 5 were excitatory pyramidal neurons and 10.4 % within layer 2/3 and the 4.6 % within layer 5 were interneurons. The interneurons comprise fast spiking cells, bitufted cells, Martinotti cells and basket cells [46]. The underlying neuron model used here was the simplified adaptive exponential integrate-and-fire neuron (simpAdEx) model shown in Eq. 6 and 7 proposed Hertaeg and colleagues [50].

$$C \cdot \frac{\mathrm{d}V}{\mathrm{d}t} = -g_L \cdot (V - E_L) + g_L \cdot \Delta_T \cdot e^{\left(\frac{V - V_T}{\Delta_T}\right)} + I - w =: w_V - w \tag{6}$$

$$\frac{\mathrm{d}w}{\mathrm{d}t} = \begin{cases} 0 & \text{for } |w - w_V| > \frac{\tau_m}{\tau_w} w_V \\ \Theta\left(V_T - V\right) \cdot \left[1 - \frac{\tau_m}{\tau_w}\right] \frac{\mathrm{d}w_V}{\mathrm{d}V} \frac{\mathrm{d}V}{\mathrm{d}t} & \text{otherwise} \end{cases} \tag{7}$$

$$\text{if } V > V_{\text{up}} \text{ then } V \to V_r \text{ and } w \to w_r = w + b$$
$$\text{if } w = \left(1 + \frac{\tau_m}{\tau_w}\right) w_V \text{ then } w \to \left(1 - \frac{\tau_m}{\tau_w}\right) w_V$$

1000 simpAdEx neurons were modelled with parameters randomly drawn from experimentally validated distributions and pairwise connection probabilities from literature [46]. Synaptic connectivities were simulated by conductance-based double exponential functions for AMPA-, $\mathrm{GABA_B}$- and NMDA-type synapses. Additionally, the synaptic models include short-term plasticity dynamics [69] with parameters drawn from separate normal distributions for short term facilitation (termed E1 for excitatory and I1 for inhibitory synapses), short term depression (E2/I2) and a combined version of both (E3/I3) [39, 97]. The cell types of the pre- and postsynaptic neurons determine which of these classes is used for each individual combination. In particular, connections among pyramidal cells, among interneurons and between fast-spiking interneurons and pyramidal exhibit all three types of connections to varying degrees (pyramidal to pyramidal: 45% E1, 38% E2, 17% E3 [97]; interneuron to interneuron: 29% E1, 58% E2, 13% E3 [39], fast-spiking interneuron to pyramidal: 25% E1, 50% E2, 25% E3 [39]). A constant background current of $I_{\text{exc}} = 250\,\text{pA}$ was applied to excitatory neurons and a current of $I_{\text{inh}} = 200\,\text{pA}$ to inhibitory neurons. For more details, see [46].

The model was supplemented with $\mathrm{GABA_B}$-type synapses to simulate the slow IPSPs, which were found to be important within the state-space model [13]. The synaptic parameters for the conductance-based double exponential functions of $\mathrm{GABA_B}$ were extracted from Golomb et al. [34] and presented in Table 7. The peak conductance of $\mathrm{GABA_A}$ and $\mathrm{GABA_B}$ were additionally reduced by multiplying with a factor of 0.3 to counteract the excess of inhibition within the network.

Table 7. Synaptic parameters of $\mathrm{GABA_B}$.

Synaptic Parameters	values
E_{rev}	$-90\,\text{mV}$
$\tau_{\text{on,GABA}_B}$	$100\,\text{ms}$
$\tau_{\text{off,GABA}_B}$	$200\,\text{ms}$
$g_{\text{peak,GABA}B}$	$\frac{1}{5} \cdot g_{\text{peak,GABA}_A} = 0.2\,\text{nS}$

To test timing within the PFC model, the full network as shown in Fig. 1 within the gray box was stimulated in the beginning and in the end of time intervals with a step current of $I_s = 220\,\text{pA}$ for $10\,\text{ms}$ to test various inter stimulus intervals $\vec{\Delta t}$. The model should ideally predict the presented inter stimulus interval. All simulations were performed with the NEST Simulator (version: 2.18.0 [54]) after extracting the parameters from MATLAB R2020a [46].

Training the network

After running the simulations, we extracted the states of all neurons ($N = 1000$) within a given time window Δt_w following the readout mechanisms of a liquid state machine [55, 68] (cf. Fig. 1). Specifically, the states in the PFC network were calculated using a sum over spikes within a small time window Δt_w that ends t_{w_2} ms after the second stimulation (Fig. 20A) in which each spike is weighted using an exponential decay rate τ^{-1}, see Eq. 8. As τ gets smaller, the spikes which occur in the end of the window are weighted stronger, and if $\tau \to \infty$, the spikes of each neuron within the window are counted without any weighting.

$$\mathrm{s} = \sum_{\substack{t_i \in \text{Spiketrain,} \\ \text{s.t. } t_1 < t_i < t_2}} \exp\left(-(t_2 - t_i)/\tau\right) \tag{8}$$

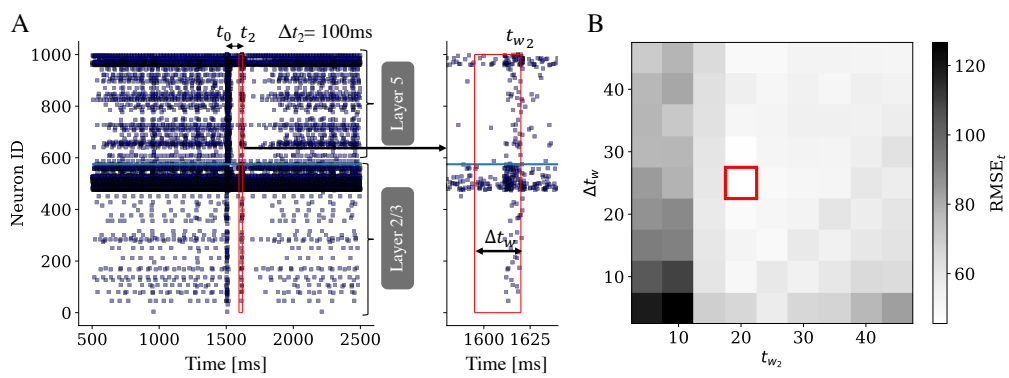

Fig 20. Extracting the states by defining a window. A. Rasterplot of all 1000 neurons with two stimulations ($t_0 = 1500\,\text{ms}$, $t_2 = 1610\,\text{ms}$) to reproduce an interval of $\Delta t_2 = 100\,\text{ms}$. The red box identifies the window in which the states from the spiketrains are extracted (right: zoomed-in view). **B**. Result of a grid search to find the optimal parameters for the window with varying window size and end time. The best parameter set was selected by the minimum RMSE-value (red box).

To predict interval durations, a readout layer was added to the model with the number of output units N_r matching the number of interval durations presented during training, cf. color-coded readout units in Fig. 1. Each output unit is then trained to be active for the respective time interval and to be inactive for all other time intervals. The readout weights were trained for all stimulus intervals and trials by maximizing the activity of the readout units for their corresponding stimulus intervals and minimizing for the remaining stimulus intervals.

Training of readout weights was realized by calculating the least squares to the expected targets, cf. Fig. 1. After training with 300 trials, the performance of time estimation was tested by presenting test intervals in $25\,\text{ms}$ steps from $50\,\text{ms}$ up to $750\,\text{ms}$ and calculating the outputs of the previously trained readout weights. To predict the interval durations of the presented inter stimulus intervals, the negative output

values were set to 0, normalized by the sum of all readout neurons, multiplied by the respective training time intervals and summed across all readout units. The standard deviation of the estimated time was calculated over $N_{\text{test,trials}} = 50$ test trials. Including the negative output values in the estimate did not significantly change the results.

The hyperparameters that determine the states are the end point t_{w_2} and the length of the window Δt_w of which spikes were extracted, and the exponential weight decay rate τ. These parameters were selected using a grid search and optimizing for minimal root mean squared error RMSE_t between the subjective and the objective time over a subset of training intervals ($N_{\text{train, trials}} = 50$) - see Fig. 20B. In a first coarse grid search, we found $\tau \to \infty$, effectively summing up the spikes within the window, to give lowest RMSE_t for all settings of the other two parameters. Therefore, we fixed $\tau \to \infty$ and further optimized the two parameters Δt_w and t_{w_2} in a finer scale grid search depicted in Fig. 20B. The optimal parameter sets were selected by the minimum root mean squared error $\langle \text{RMSE}_t \rangle_{\textbf{trials}} = 45.6\,\text{ms}$ with $\Delta t_w = 25\,\text{ms}$, $t_{w_2} = 20\,\text{ms}$ and $\tau \to \infty$ as indicated by the red box in Figs. 20A, B.

Dopaminergic modulation

The agonistic and antagonistic D2 receptor modulations were simulated by modifying various neuronal and synaptic properties. To alter neuronal parameters, we extracted the changes from own unpublished data, in which the D2 receptor agonist, quinpirole, [23] was applied with a concentration of $10\,\mu$M. In contrast to that, the changes of synaptic conductance were extracted from literature (for more details, see Table 8). Specifically, we interpreted the changes on neuronal and synaptic modulation under the application of dopamine as 100 % agonistic modulation, cf. Table 8, the properties without application of dopamine as 0 % modulation and linearly interpolated between these two. Similarly, we extrapolated from 0 % to −100 % to simulate the antagonistic modulation via dopamine. In order to simulate the acute change in neuronal activity induced by dopamine, we applied the modulation at test time without retraining the readout weights. To examine long-term plasticity-based adaptions induced by dopamine, we also retrained the readout weights in a second step for the case of ±30 % agonistic and antagonistic modulation.

Table 8. Parameter alterations for D2 modulation.

Parameters		change	literature
Neuronal parameters			
Reset potential	V_r	-5.2%	
Threshold	V_{th}	-3.7%	
Capacity	C_m	+1.2%	
Leak conductance	g_L	-14.2%	
Leak reversial potenital	E_L	+6.6%	
Delta T	sf	+ 27.8%	
Peak Potential	V_{peak}	-4.1%	
adaptation time constant	t_{cw}	-14.2%	
spike-triggeried adaptation	b	+ 9.8%	
Synaptic parameters			
Peak conductance NMDA	g_{NMDA}	-20%	[62, 84, 105]
Peak conductance GABA	g_{GABA}	-50%	[85]

Noise

To simulate variability across trials, an input layer of 10 Poisson neurons was added, such that each PFC neuron on average received input from one Poisson neuron with a firing rate of 1 Hz. As a typical cortical neuron receives connections from approximately 1000-10 000 other neurons [8, 75], we examined the effect of higher input variability in our model by increasing the firing rates of our Poisson process to 1000 Hz, thereby emulating 1000 additional inputs. To test different noise levels, we increased the synaptic weights of the Poisson neurons, and in parallel reduced the background current to $(-7\,\%, -21\,\%, -36\,\%, -50\,\%)$ of the default to compensate over excitation. Specifically, for each synaptic weight factor, the background current was optimized using a grid search to minimize RMSE of averaged firing rates per neuron type and layer.

The time averaged sub-threshold membrane potential fluctuation, i.e. after removal of spikes, was shown to be at 4 mV in experiments [17], which could already be reproduced within the PFC model [46]. For decreased background current and accordingly increased noise levels as described above, we find that sub-threshold membrane potential fluctuations are within the range of $2-4$ mV.

Analysis methods

Rheobase

The excitability of each PFC neuron was determined by the rheobase I_{rheo} as proposed by Hertaeg and colleagues [50] as shown in Eq. 9.

$$I_{\text{rheo}} = (a + g_L) \cdot \left[V_T - E_L - \Delta_T + \Delta_T \cdot \ln\left(1 + \frac{a}{g_L}\right)\right] \tag{9}$$

Defining interval encoding pools

In order to understand which intrinsic mechanisms were key features for the differentiation within training, we classified a neuron according to its highest readout weight contribution to its corresponding trained intervals as was already done in [13]. After classifying, the same neuron will not be considered for the remaining readout neurons. These neurons were sorted according to the corresponding interval encoding pool, see Fig. 8A. Only neurons with positive readout weights of above 0.01 are considered to examine the functional role of these neurons for training.

Sequential activation of pools

After defining the interval encoding pools, we examined whether there was a sequential activation of the pools from lower intervals to higher intervals. For this, we calculated the summed synaptic weights from the presynaptic lower intervals to a subsequent postsynaptic interval encoding neuron (cf. Fig 19A), normalized by the overall synaptic weight the neuron receives from all neurons and averaged over all postsynaptic neurons. The synaptic correlation activations between the pools were computed for all interval combinations and not only for the subsequent pools.

Minimal model

In order to further understand how the firing rate of the network changes over time, we have constructed a minimal model comprising a single neuron that is subject to the same synaptic currents and external inputs that are present in the full model. The neuron is modelled as a leaky integrate-and-fire neuron with parameters that are identical to the average values for a L23 pyramidal cell in the full model (C=170 pF,

g_L=5.85 nS, E_L=−75.5 mV, V_{th}=−65 mV). AMPA, $GABA_A$, NMDA and $GABA_B$ synapses are modelled as in the full model (without STP). Except for $GABA_B$, all synapses are stimulated by a Poisson spike train with $\lambda = 0.25$, simulating random spike trains at 4000 Hz for both the excitatory and inhibitory synapses, balancing excitation and inhibition. The $GABA_B$ synapse is stimulated by 20 spikes during the first 20 ms of the simulation to mimic the first stimulus that marks the beginning of the interval. The neuron is subject to a constant background current of 40 pA, which is raised to 90 pA for 20 ms at the time of the second stimulus. The interval duration is varied between 50 and 500 ms in steps of 25 ms . We simulated $N = 100$ independent neurons and computed the mean and standard deviation of the membrane potential over all neurons at each of these durations. Assuming a normal distribution of the membrane potential, we then computed the probability p of the membrane potential to exceed the firing threshold V_{th} and interpreted $N * p$ as the firing rate at a given time, which is depicted in Fig. 17. The different curves in this figure were generated by varying V_{th} between −67 and −63 mV in steps of 0.1 mV. Similar results are obtained by simply counting the number of neurons exceeding V_{th} in each case.

Acknowledgments

We are grateful to Prof. Dr. Daniel Durstewitz (Central Institute of Mental Health, Mannheim) for providing us with advice and computational resources. We would also like to thank Dr. Jakob Jordan (Department of Physiology, University of Bern, Switzerland) for his help in implementing the neuron model in NEST and Dr. Tatiana Golovko (Central Institute of Mental Health, Mannheim) for collecting the dopaminergic modulation data. The authors acknowledge the support by the state of Baden-Württemberg through bwHPC.

References

1. L. G. Allan. The perception of time. *Perception & psychophysics*, 26(5):340–354, 1979.

2. M. J. Allman and W. H. Meck. Pathophysiological distortions in time perception and timed performance. *Brain*, 135(3):656–677, 2012.

3. R. Almeida and A. Ledberg. A biologically plausible model of time-scale invariant interval timing. *J Comput Neurosci*, 28:155–175, 2010.

4. L. A. Bizo, J. Y. Chu, F. Sanabria, and P. R. Killeen. The failure of weber's law in time perception and production. *Behavioural processes*, 71(2-3):201–210, 2006.

5. D. A. Blankenship and N. H. Anderson. Subjective duration: A functional measurement analysis. *Perception & Psychophysics*, 20(3):168–172, 1976.

6. D. J. Bobko, H. R. Schiffman, R. J. Castino, and W. Chiappetta. Contextual effects in duration experience. *The American journal of psychology*, pages 577–586, 1977.

7. M. Bortoletto, A. Cook, and R. Cunnington. Motor timing and the preparation for sequential actions. *Brain and cognition*, 75(2):196–204, 2011.

8. V. Braitenberg and A. Schüz. *Anatomy of the cortex: statistics and geometry*, volume 18. Springer Science & Business Media, 2013.

9. C. D. Brody, A. Hernández, A. Zainos, and R. Romo. Timing and neural encoding of somatosensory parametric working memory in macaque prefrontal cortex. *Cerebral cortex*, 13(11):1196–1207, 2003.

10. A. Brown and S. Gershon. Dopamine and depression. *Journal of Neural Transmission/General Section JNT*, 91(2):75–109, 1993.

11. C. V. Buhusi and W. H. Meck. What makes us tick? functional and neural mechanisms of interval timing. *Nature reviews neuroscience*, 6(10):755–765, 2005.

12. C. V. Buhusi, M. B. Reyes, C.-A. Gathers, S. A. Oprisan, and M. Buhusi. Inactivation of the medial-prefrontal cortex impairs interval timing precision, but not timing accuracy or scalar timing in a peak-interval procedure in rats. *Frontiers in integrative neuroscience*, 12:20, 2018.

13. D. V. Buonomano. Decoding temporal information: a model based on short-term synaptic plasticity. *Journal of Neuroscience*, 20(3):1129–1141, 2000.

14. D. V. Buonomano. Neural dynamics based timing in the subsecond to seconds range. *Neurobiology of interval timing*, pages 101–117, 2014.

15. D. V. Buonomano and W. Maass. State-dependent computations: spatiotemporal processing in cortical networks. *Nature Reviews Neuroscience*, 10 (2):113–125, 2009.

16. M. B. Cantor and J. F. Wilson. Temporal uncertainty as an associative metric: Operant simulations of pavlovian conditioning. *Journal of Experimental Psychology: General*, 110(2):232, 1981.

17. A. Destexhe, M. Rudolph, J.-M. Fellous, and T. J. Sejnowski. Fluctuating synaptic conductances recreate in vivo-like activity in neocortical neurons. *Neuroscience*, 107(1):13–24, 2001.

18. S. Droit-Volet. Time perception, emotions and mood disorders. *Journal of Physiology-Paris*, 107(4):255–264, 2013.

19. B. W. Dunlop and C. B. Nemeroff. The role of dopamine in the pathophysiology of depression. *Archives of general psychiatry*, 64(3):327–337, 2007.

20. D. Durstewitz. Self-organizing neural integrator predicts interval times through climbing activity. *Journal of Neuroscience*, 23(12):5342–5353, 2003.

21. D. Durstewitz, J. K. Seamans, and T. J. Sejnowski. Dopamine-mediated stabilization of delay-period activity in a network model of prefrontal cortex. *J Neurophysiol*, 83:1733–1750, 2000.

22. D. M. Eagleman. Human time perception and its illusions. *Current opinion in neurobiology*, 18(2):131–136, 2008.

23. D. Eilam, I. Golani, and H. Szechtman. D2-agonist quinpirole induces perseveration of routes and hyperactivity but no perseveration of movements. *Brain research*, 490(2):255–267, 1989.

24. H. Eisler. Subjective duration and psychophysics. *Psychological Review*, 82(6): 429, 1975.

25. H. Eisler. Experiments on subjective duration 1868-1975: A collection of power function exponents. *Psychological Bulletin*, 83(6):1154, 1976.

26. S. Escola, M. Eisele, K. Miller, and L. Paninski. Maximally reliable markov chains under energy constraints. *Neural computation*, 21(7):1863–1912, 2009.

27. J. G. Fetterman and P. R. Killeen. Time discrimination in columba livia and homo sapiens.. *Journal of Experimental Psychology: Animal Behavior Processes*, 18(1):80, 1992.

28. V. Franssen, A. Vandierendonck, and A. Van Hiel. Duration estimation and the phonological loop: Articulatory suppression and irrelevant sounds. *Psychological research*, 70(4):304–316, 2006.

29. C. R. Gallistel and J. Gibbon. Time, rate, and conditioning. *Psychological review*, 107(2):289, 2000.

30. D. J. Getty. Discrimination of short temporal intervals: A comparison of two models. *Perception & psychophysics*, 18(1):1–8, 1975.

31. J. Gibbon. Scalar expectancy theory and weber's law in animal timing. *Psychological review*, 84(3):279, 1977.

32. J. Gibbon, C. Malapani, C. L. Dale, and C. R. Gallistel. Toward a neurobiology of temporal cognition: advances and challenges. *Curr. Opin. Neuro.*, 7:170–184, 1997.

33. S. Glasauer and Z. Shi. The origin of vierordt's law: The experimental protocol matters. *PsyCh Journal*, 2021.

34. D. Golomb, X.-J. Wang, and J. Rinzel. Synchronization properties of spindle oscillations in a thalamic reticular nucleus model. *Journal of neurophysiology*, 72 (3):1109–1126, 1994.

35. S. Grondin. From physical time to the first and second moments of psychological time. *Psychological bulletin*, 127(1):22, 2001.

36. S. Grondin. Timing and time perception: a review of recent behavioral and neuroscience findings and theoretical directions. *Attention, Perception, & Psychophysics*, 72(3):561–582, 2010.

37. S. Grondin. Unequal weber fractions for the categorization of brief temporal intervals. *Attention, Perception, & Psychophysics*, 72(5):1422–1430, 2010.

38. S. Grossberg and N. A. Schmajuk. Neural dynamics of adaptive timing and temporal discrimination during associative learning. *Neural Networks*, 2(2): 79–102, 1989.

39. A. Gupta, Y. Wang, and H. Markram. Organizing principles for a diversity of gabaergic interneurons and synapses in the neocortex. *Science*, 287(5451): 273–278, 2000.

40. A. R. Halpern and C. J. Darwin. Duration discrimination in a series of rhythmic events. *Perception & Psychophysics*, 31(1):86–89, 1982.

41. J. Hass and D. Durstewitz. Neurocomputational models of time perception. *Neurobiology of interval timing*, pages 49–71, 2014.

42. J. Hass and D. Durstewitz. Time at the center, or time at the side? assessing current models of time perception. *Current Opinion in Behavioral Sciences*, 8: 238–244, 2016.

43. J. Hass and J. M. Herrmann. The neural representation of time: An information-theoretic perspective. *Neural Computation*, 24(6):1519–1552, 2012.

44. J. Haß, S. Blaschke, T. Rammsayer, and J. M. Herrmann. A neurocomputational model for optimal temporal processing. *Journal of computational neuroscience*, 25(3):449–464, 2008.

45. J. Hass, S. Blaschke, and J. M. Herrmann. Cross-modal distortion of time perception: demerging the effects of observed and performed motion. *PloS one*, 7(6):e38092, 2012.

46. J. Hass, L. Hertäg, and D. Durstewitz. A detailed data-driven network model of prefrontal cortex reproduces key features of in vivo activity. *PLoS computational biology*, 12(5):e1004930, 2016.

47. J. Hass, S. Ardid, J. Sherfey, and N. Kopell. Constraints on persistent activity in a biologically detailed network model of the prefrontal cortex with heterogeneities. *Progress in Neurobiology*, 215:102287, 2022.

48. J. Hass, S. Ardid, J. Sherfey, and N. Kopell. Constraints on persistent activity in a biologically detailed network model of the prefrontal cortex with heterogeneities. *Progress in Neurobiology*, 215:102287, 2022.

49. J. Henderson, T. A. Hurly, M. Bateson, and S. D. Healy. Timing in free-living rufous hummingbirds, selasphorus rufus. *Current biology*, 16(5):512–515, 2006.

50. L. Hertäg, J. Hass, T. Golovko, and D. Durstewitz. An approximation to the adaptive exponential integrate-and-fire neuron model allows fast and predictive fitting to physiological data. *Frontiers in computational neuroscience*, 6:62, 2012.

51. O. D. Howes, R. McCutcheon, M. J. Owen, and R. M. Murray. The role of genes, stress, and dopamine in the development of schizophrenia. *Biological psychiatry*, 81(1):9–20, 2017.

52. R. B. Ivry and J. E. Schlerf. Dedicated and intrinsic models of time perception. *Trends in cognitive sciences*, 12(7):273–280, 2008.

53. C. R. Jones, K. Rosenkranz, J. C. Rothwell, and M. Jahanshahi. The right dorsolateral prefrontal cortex is essential in time reproduction: an investigation with repetitive transcranial magnetic stimulation. *Experimental Brain Research*, 158(3):366–372, 2004.

54. J. Jordan, R. Deepu, J. Mitchell, J. M. Eppler, S. Spreizer, J. Hahne, E. Thomson, I. Kitayama, A. Peyser, T. Fardet, et al. Nest 2.18. 0. Technical report, Jülich Supercomputing Center, June 2019. URL https://zenodo.org/record/2605422.

55. J. Kaiser, R. Stal, A. Subramoney, A. Roennau, and R. Dillmann. Scaling up liquid state machines to predict over address events from dynamic vision sensors. *Bioinspiration & biomimetics*, 12(5):055001, 2017.

56. R. Kanai, C. L. Paffen, H. Hogendoorn, and F. A. Verstraten. Time dilation in dynamic visual display. *Journal of vision*, 6(12):8–8, 2006.

57. S. Kaneko and I. Murakami. Perceived duration of visual motion increases with speed. *Journal of Vision*, 9(7):14–14, 2009.

58. K. Kang, M. Shelley, and H. Sompolinsky. Mexican hats and pinwheels in visual cortex. *Proceedings of the National Academy of Sciences*, 100(5):2848–2853, 2003.

59. U. R. Karmarkar and D. V. Buonomano. Timing in the absence of clocks: Encoding time in neural network states. *Neuron*, 53(3):427–438, 2007.

60. J. Kim, A. H. Jung, J. Byun, S. Jo, and M. W. Jung. Inactivation of medial prefrontal cortex impairs time interval discrimination in rats. *Frontiers in behavioral neuroscience*, 3:38, 2009.

61. G. Koch, M. Oliveri, S. Torriero, and C. Caltagirone. Underestimation of time perception after repetitive transcranial magnetic stimulation. *Neurology*, 60(11): 1844–1846, 2003.

62. S. A. Kotecha, J. N. Oak, M. F. Jackson, Y. Perez, B. A. Orser, H. H. Van Tol, and J. F. MacDonald. A d2 class dopamine receptor transactivates a receptor tyrosine kinase to inhibit nmda receptor transmission. *Neuron*, 35(6):1111–1122, 2002.

63. C. C. Lapish, S. Kroener, D. Durstewitz, A. Lavin, and J. K. Seamans. The ability of the mesocortical dopamine system to operate in distinct temporal modes. *Psychopharmacology*, 191(3):609–625, 2007.

64. H. Lejeune and J. H. Wearden. Vierordt's the experimental study of the time sense (1868) and its legacy. *European Journal of Cognitive Psychology*, 21(6): 941–960, 2009.

65. M. I. Leon and M. N. Shadlen. Representation of time by neurons in the posterior parietal cortex of the macaque. *Neuron*, 38(2):317–327, 2003.

66. P. A. Lewis and R. C. Miall. Remembering the time: a continuous clock. *Trends in cognitive sciences*, 10(9):401–406, 2006.

67. P. A. Lewis and R. C. Miall. The precision of temporal judgement: milliseconds, many minutes, and beyond. *Philosophical Transactions of the Royal Society B: Biological Sciences*, 364(1525):1897–1905, 2009.

68. W. Maass, T. Natschläger, and H. Markram. Real-time computing without stable states: A new framework for neural computation based on perturbations. *Neural computation*, 14(11):2531–2560, 2002.

69. H. Markram, Y. Wang, and M. Tsodyks. Differential signaling via the same axon of neocortical pyramidal neurons. *Proceedings of the National Academy of Sciences*, 95(9):5323–5328, 1998.

70. M. S. Matell and W. H. Meck. Cortico-striatal circuits and interval timing: coincidence detection of oscillatory processes. *Cognitive brain research*, 21(2): 139–170, 2004.

71. W. H. Meck. Affinity for the dopamine d2 receptor predicts neuroleptic potency in decreasing the speed of an internal clock. *Pharmacology Biochemistry and Behavior*, 25(6):1185–1189, 1986.

72. H. Y. Meltzer and S. M. Stahl. The dopamine hypothesis of schizophrenia: a review. *Schizophrenia bulletin*, 2(1):19, 1976.

73. H. Merchant and V. De Lafuente. Introduction to the neurobiology of interval timing. *Neurobiology of interval timing*, pages 1–13, 2014.

74. C. Miall. The storage of time intervals using oscillating neurons. *Neural Computation*, 1(3):359–371, 1989.

75. J. M. Murre and D. P. Sturdy. The connectivity of the brain: multi-level quantitative analysis. *Biological cybernetics*, 73(6):529–545, 1995.

76. A. Nani, J. Manuello, D. Liloia, S. Duca, T. Costa, and F. Cauda. The neural correlates of time: a meta-analysis of neuroimaging studies. *Journal of Cognitive Neuroscience*, 31(12):1796–1826, 2019.

77. N. S. Narayanan. Ramping activity is a cortical mechanism of temporal control of action. *Current opinion in behavioral sciences*, 8:226–230, 2016.

78. H. Onoe, M. Komori, K. Onoe, H. Takechi, H. Tsukada, and Y. Watanabe. Cortical networks recruited for time perception: a monkey positron emission tomography (pet) study. *Neuroimage*, 13(1):37–45, 2001.

79. F. H. Petzschner, S. Glasauer, and K. E. Stephan. A bayesian perspective on magnitude estimation. *Trends in cognitive sciences*, 19(5):285–293, 2015.

80. I. Polti, B. Martin, and V. van Wassenhove. The effect of attention and working memory on the estimation of elapsed time. *Scientific reports*, 8(1):1–11, 2018.

81. S. Rahman, J. Zhang, E. Engleman, and W. Corrigall. Neuroadaptive changes in the mesoaccumbens dopamine system after chronic nicotine self-administration: a microdialysis study. *Neuroscience*, 129(2):415–424, 2004.

82. T. Rammsayer. Temporal discrimination in schizophrenic and affective disorders: evidence for a dopamine-dependent internal clock. *International Journal of Neuroscience*, 53(2-4):111–120, 1990.

83. T. Rammsayer, P. Netter, and W. H. Vogel. A neurochemical model underlying differences in reaction times between introverts and extraverts. *Personality and Individual Differences*, 14(5):701–712, 1993.

84. J. K. Seamans and C. R. Yang. The principal features and mechanisms of dopamine modulation in the prefrontal cortex. *Progress in neurobiology*, 74(1): 1–58, 2004.

85. J. K. Seamans, N. Gorelova, D. Durstewitz, and C. R. Yang. Bidirectional dopamine modulation of gabaergic inhibition in prefrontal cortical pyramidal neurons. *Journal of Neuroscience*, 21(10):3628–3638, 2001.

86. Z. Shi, R. M. Church, and W. H. Meck. Bayesian optimization of time perception. *Trends in cognitive sciences*, 17(11):556–564, 2013.

87. P. Simen, F. Balci, L. deSouza, J. D. Cohen, and P. Holmes. A model of interval timing by neural integration. *Journal of Neuroscience*, 31(25):9238–9253, 2011.

88. G. B. Smith, B. Hein, D. E. Whitney, D. Fitzpatrick, and M. Kaschube. Distributed network interactions and their emergence in developing neocortex. *Nature neuroscience*, 21(11):1600–1608, 2018.

89. R. Spanagel and F. Weiss. The dopamine hypothesis of reward: past and current status. *Trends in neurosciences*, 22(11):521–527, 1999.

90. S. Stevens. Psychophysics: Introduction to its perceptual, neural, and social prospects. 2000 ed. *New York: John Willey and Sons*, 1975.

91. S. Thönes and D. Oberfeld. Time perception in depression: A meta-analysis. *Journal of Affective Disorders*, 175:359–372, 2015.

92. N. Ueda, K. Maruo, and T. Sumiyoshi. Positive symptoms and time perception in schizophrenia: A meta-analysis. *Schizophrenia Research: Cognition*, 13:3–6, 2018.

93. G. E. Uhlenbeck and L. S. Ornstein. On the theory of the brownian motion. *Physical review*, 36(5):823, 1930.

94. C. Van Vreeswijk and H. Sompolinsky. Chaos in neuronal networks with balanced excitatory and inhibitory activity. *Science*, 274(5293):1724–1726, 1996.

95. V. Van Wassenhove, D. V. Buonomano, S. Shimojo, and L. Shams. Distortions of subjective time perception within and across senses. *PloS one*, 3(1):e1437, 2008.

96. K. Vierordt. *Der zeitsinn nach versuchen*. H. Laupp, 1868.

97. Y. Wang, H. Markram, P. H. Goodman, T. K. Berger, J. Ma, and P. S. Goldman-Rakic. Heterogeneity in the pyramidal network of the medial prefrontal cortex. *Nature neuroscience*, 9(4):534–542, 2006.

98. J. H. Wearden, H. Edwards, M. Fakhri, and A. Percival. Why"sounds are judged longer than lights": Application of a model of the internal clock in humans. *The Quarterly Journal of Experimental Psychology: Section B*, 51(2):97–120, 1998.

99. M. Wiener, P. Turkeltaub, and H. B. Coslett. The image of time: a voxel-wise meta-analysis. *Neuroimage*, 49(2):1728–1740, 2010.

100. H. Woodrow. The reproduction of temporal intervals. *Journal of Experimental Psychology*, 13(6):473, 1930.

101. H. Woodrow. The temporal indifference interval determined by the method of mean error. *Journal of Experimental Psychology*, 17(2):167, 1934.

102. M. Xu, S.-y. Zhang, Y. Dan, and M.-m. Poo. Representation of interval timing by temporally scalable firing patterns in rat prefrontal cortex. *Proceedings of the National Academy of Sciences*, 111(1):480–485, 2014.

103. A. D. Yarmey. Retrospective duration estimations for variant and invariant events in field situations. *Applied Cognitive Psychology: The Official Journal of the Society for Applied Research in Memory and Cognition*, 14(1):45–57, 2000.

104. K. Yc, L. Prado, and H. Merchant. The scalar property during isochronous tapping is disrupted by a d2-like agonist in the nonhuman primate. *Journal of Neurophysiology*, 121(3):940–949, 2019.

105. P. Zheng, X.-X. Zhang, B. Bunney, and W.-X. Shi. Opposite modulation of cortical n-methyl-d-aspartate receptor-mediated responses by low and high concentrations of dopamine. *Neuroscience*, 91(2):527–535, 1999.